DEPARTMENT OF PHYSICS

TECHNICAL UNIVERSITY OF MUNICH

Bachelor's Thesis in Physics

Beam deflection by a stack of mosaic crystals

Cemil Görkem Tamer

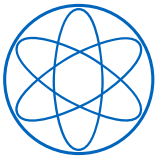

DEPARTMENT OF PHYSICS

TECHNICAL UNIVERSITY OF MUNICH

Bachelor's Thesis in Physics

Beam deflection by a stack of mosaic crystals

Strahlumlenkung durch einen Stapel von Mosaikkristallen

Author:	Cemil Görkem Tamer
Supervisor:	Dr. Joachim Wuttke
Advisor:	Dr. Joachim Wuttke
Submission Date:	August 27, 2025

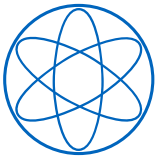

I confirm that this bachelor's thesis in physics is my own work and I have documented all sources and material used.

Munich, August 27, 2025 Cemil Görkem Tamer

Abstract

This work presents the development and critical evaulation of a computational framework for modeling neutron scattering on mosaic crystals, with particular focus on applications to phase-space transformation (PST) choppers in backscattering spectrometers such as SPHERES at FRM II [1]. The formalism builds on the construction of Bragg matrices, which describe scattering probabilites on a discretized angular grid, and extends it to account for tilted crystals and multi crystal stack configurations, from an existing formalism and implementation for single crystals [2].

The tilted crystal formulation is verified by analyzing the deflection and azimuthal-shift functions, confirming their correct implementation in the angular grid. However, the construction of the Bragg matrix for tilted crystals reveals duplicate entries that violate probability conservation, leading to unphysical attenuation and unreliable reflectivity curves. These inconsistencies are shown to originate from implementation issues rather than the theoretical framework itself, highlighting the need for refinement of the reflection kernel and binning methods.

A stack model for multiple crystals is also introduced to capture transmission and reflection through layered systems. While the model ensures partial flux continuity via coupling vectors, the absence of a proper reflection-coupling element prevents the recovery of backward-propagating flux, resulting in incomplete reflectivity and transmission data. This limitation underscores the importance of incorporating interfacial reflection to achieve a consistent multi-crystal description.

The results establish both the strengths and current shortcomings of the framework. On the one hand, the model successfully reproduces angularly resolved scattering distributions and captures the expected shifts of Bragg conditions under crystal tilting. On the other, implementation-level errors hinder probability conservation, and the lack of reflection coupling restricts the applicability to realistic multi-layer systems.

Outlook is given toward refining the Bragg matrix construction for tilted crystals, introducing reflection coupling into the stack model, and unifying the two approaches into a single framework capable of simulating a static PST chopper. This would form the basis for future simulations of a rotating PST chopper, thereby bridging the gap between theoretical modeling and experimental implementation in neutron backscattering spectroscopy.

Contents

1 Introduction

Neutron scattering is an essential tool in the study of material dynamics, offering unique insights that are often inaccessible through other experimental techniques. Neutrons, being electrically neutral, can penetrate deep into matter without significantly disturbing the sample, making them ideal for probing bulk properties. Their wavelength and energy scales are well-matched to atomic and molecular motions, allowing precise investigation of structural and dynamical phenomena. Neutron backscattering spectroscopy, in particular enables the measurement of extremely small energy transfers with high resolution, making it invaluable for studying slow dynamics such as diffusive motion, molecular rotations, and low-energy excitations in solids and liquids [3, 4, 5, 6, 7, 8, 9, 10]. These capabilities are especially crucial in fields such as soft matter physics, solid-state ionics, and materials chemistry, where understanding the microscopic dynamics is key to advancing applications in batteries, fuel cells , and polymers [11, 12, 13].

Neutrons for research purposes are typically generated either in low-enriched uranium reactors or with other processes, with their energies subsequently moderated using materials such as water, beryllium, or graphite to achieve thermal, cold, or ultracold neutron regimes. The energy and velocity of neutrons determine their classification, while their de Bronglie wavelength enables wave-like interactions with matter, forming the basis of diffraction experiments. Elastic neutron scattering, exemplified by neutron diffraction and reflectometry, preserves the neutron's energy while providing high-resolution structural information. Compared to X-ray diffraction, neutrons offer advantages such as sensitivity to light elements, specially to hydrogen, and the ability to probe larger scattering angles, though larger sample sizes are typically required. In contrast, inelastic neutron scattering involves energy transfer between neutrons and the sample, providing spectroscopic insight into atomic and molecular dynamics. Techniques include time-of-flight scattering, neutron backscattering, neutron spin echo, and triple-axis spectrometry, enabling studies of phonons, molecular reorientations, and diffusive processes with energy resolutions ranging from milli- to nanoelectron-volts. These methods have become fundamental in condensed matter physics, a significance recognized by the 1994 Nobel Prize awarded to Shull and Brockhouse for their pioneering development of neutron diffraction and spectroscopy techniques [14].

In earlier designs, neutron backscattering spectrometers typically employed a straight-

forward configuration of stationary monochromators and analyzer crystals, combined with a mechanical Doppler drive for energy scanning. In such systems, the incoming neutron beam is directed onto a monochromator crystal, which, through Bragg reflection at angles close to 90° (the so-called backscattering geometry), selects neutrons with an extremely narrow energy distribution. These monochromated neutrons interact with the sample, where inelastic scattering processes induce slight energy changes corresponding to atomic or molecular motions. The scattered neutrons are then analyzed by a second crystal, also positioned in near-backscattering geometry, ensuring that only neutrons with energies nearly identical to the incident ones are reflected toward the detector. To probe a small energy range around the nominal energy, the spectrometer employs a Doppler-driven monochromator or alternatively, controlled motion of the sample, thereby introducing a well-defined energy shift in the incident neutrons. By recording the neutron intensity as a function of this energy shift, the spectrometer produces the energy spectrum of the sample, revealing the dynamical properties at the molecular scale.

In this work, particular attention is devoted to neutron backscattering spectroscopy, with a focus on SPHERES (SPectrometer for High Energy RESolution) [1], located at the Heinz Maier-Leibnitz Zentrum (FRM II) in Munich. SPHERES is classified as a third-generation backscattering spectrometer and is employed in a wide variety of investigations, including hyperfine splitting, molecular reorientations and rotational tunneling, dynamic signatures of phase transitions, hydrogen diffusion, liquid dynamics, polymer relaxation, and protein motion [15]. The designation *third generation* refers to the use of a compact phase-space transform (PST) chopper, which unifies the functions of the primary beam deflector and duty-cycle chopper into a single component. Main objective of the primary beam deflector is to prevent the incoming and outgoing neutron paths from coinciding, while a duty-cycle chopper provides timing control to trace each detected neutron back to its origin. In addition, this design not only simplifies the overall instrument architecture but also enhances the neutron flux at the monochromator by performing a phase-space transformation of the incoming beam. A schematic illustration of SPHERES, including the neutron flight path, is presented in Figure 1.1.

Beyond its primary function, the PST chopper plays a crucial role in enhancing the neutron flux intensity, making it an indispensable element of the spectrometer architecture and a critical component to optimize for effective measurements. The design of the PST chopper consists of a rotating disk in which half of the circumference is equipped with deflector crystals that redirect the incoming beam towards the monochromator, while the other half remains open (see Figure 1.2a). When the chopper is in open position, the incoming beam is absorbed by a beam stop, whereas neutrons returning from the monochromator are transmitted towards the sample. Structurally, the PST

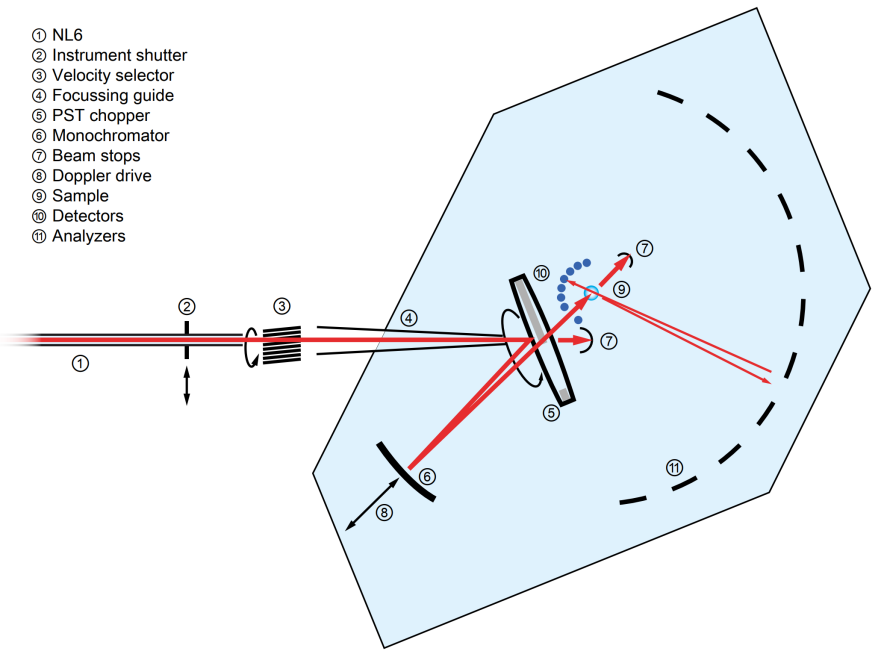

Figure 1.1: Schematic overview of the SPHERES spectrometer [16], showing its main components (numbered according to the legend) and the neutron beam path highlighted by red arrows.

chopper employs pyrolytic graphite mosaic crystals with a specified mosaicity of 2.5°. A large mosaicity is a necessity in order to deliver a sufficiently broad wavelength range to the monochromator, enabling effective spectral scans. These crystals are later arranged in stacks of three, tilted at 0°, +2.5° and -2.5°, using aluminium wedges to achieve the required orientation (see Figure 1.2b) [1].

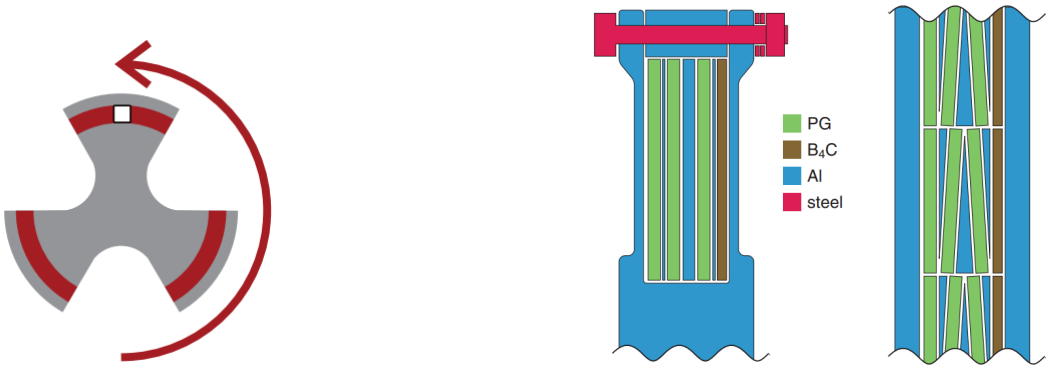

(a) (b)

Figure 1.2: Design of the PST chopper from different perspectives [1]. (a) Complete shape of the PST chopper with rotation direction indicated by the arrow, while white area shows the region where the neutron beam intersects the chopper. Red are shows the region of the deflector crystal. (b) Deflector stack inside the PST chopper: left, the cross-sectional view; right, view along the chopper axis from outside. Mosaic crystals are depicted in green, aluminium wedges in blue, and the absorber plate at the end in brown.

One of the main challenges in neutron spectroscopy is that they often require long measurement times to achieve high accuracy, and their operation can be costly in terms of not just time but also resources. As a result, determining optimal working conditions is a non-trivial task that demands careful planning and efficiency. A practical solution to this problem lies in the use of computational methods to simulate and evaulate different experimental configurations in advance. By modeling the instrument's behavior under various conditions, researchers can identify optimal parameters without the need for extensive trial-and-error in real experiments. This approach not only accelerates the setup process but also conserves valuable beam time and operational costs, making experimental campaigns significantly more efficient. In a nutshell, creating a possible "digital twin" for SPHERES might be beneficial in the future.

In this work, as the title suggests, our main objective is to investigate multi-Bragg reflection in a stack of mosaic crystals, building upon an earlier model that describes

multi-Bragg reflection in a single thick crystal [2]. In our extended approach, the system, represented as a stack of mosaic crystals, serves as a simplified model for the PST chopper used in third-generation neutron backscattering spectrometers. Specifically, the PST chopper is modeled as three back-to-back mosaic crystal layers, each with a distinct angular orientation relative to the primary plane. This layered configuration introduces additional complexity to the reflection behavior, making it essential to understand how these angular offsets influence the overall neutron deflection on the chopper.

The structure of this thesis is organized as follows: First, the existing model for multi-Bragg reflection in a single mosaic crystal will be presented and explained in detail, laying the groundwork for the subsequent developments. Next, the model will be extended to include a stack of N back-to-back mosaic crystals aligned parallel to each other, allowing for a generalized model. Following this, the tilting of each individual crystal layer with respect to the main plane will be incorporated into the model to more accurately reflect the geometry of a PST chopper. Finally, the results obtained from these extended models will be presented and discussed, with particular emphasis on how stacking and angular variation affect the reflection characteristics and overall performance of the system.

2 Theory

2.1 Reflection Model for a Single Thick Mosaic Crystal

As a starting point, the model for a single mosaic crystal will be presented, drawing on two previously established models [2, 17]. This section primarily serves to summarize the existing theoretical framework and provide the necessary foundation for extending the model to a stack of crystals. By revisiting and consolidating these earlier approaches, we establish a clear baseline from which the more complex stacked system can be systematically developed.

2.1.1 Preliminary Considerations

A mosaic crystal is a type of crystal composed of many small, slightly misaligned crystalline domains, all having nearly the same lattice structure but with small angular deviations from one another. This structure allows mosaic crystals to reflect a broader range of incident neutron angles compared to perfect crystals, making them especially useful in neutron optics for increasing the reflected intensity while maintaining good energy resolution. Each crystalline domain, named as block, is assumed to be thin enough that it reflects only a small portion of the incident beam, allowing the neglection of primary extinction and internal multiple reflections within a single block.

Since the reflections from different blocks occur incoherently, classical transport theory is chosen as the appropriate framework to describe the system [17]. The primary objective is to calculate steady-state neutron flux, expressed as the current distribution $I(\vec{k}, \vec{r})$. The analysis focuses on elastic scattering, while inelastic scattering is incorporated through a loss term that will be introduced later. Because the scattering is assumed elastic, the wavenumber $|\vec{k}|$ is considered conserved, and can be neglected completely except for its propogation direction $\hat{k}$. Furthermore, the mosaic crystal is modeled as a infinitely extended slab in the xy-plane, allowing us to neglect any spatial variation in those directions. These assumptions together reduce the problem from a six-dimensional phase space to a more tractable three-dimensional function $I(\hat{k}, z)$. This simplification enables the boundary-value problem to be addressed efficiently on a computational grid.

As previously mentioned, classical transport theory serves as the foundational

framework for this analysis. Within this context, the current distribution $I(\hat{k}, z)$ satisfies the stationary (time-independent) Boltzmann transport equation, which governs the behavior of particles undergoing scattering and absorption in a medium. The equation describes the balance between incoming and outgoing neutron flux at each point in space and direction, accounting for scattering events and losses. The stationary Boltzmann equation for $I(\hat{k}, z)$ can be written as

$$(\hat{k}_z \partial_z + A) I(\hat{k}, z) - B \circ I(\hat{k}, z) = 0, \tag{2.1}$$

where B is a linear operator describing the gain from the Bragg diffraction and A is the attenuation operator where the losses by diffraction and other factors are considered [2].

To solve Equation 2.1, appropriate boundary conditions [2] must be specified. We consider an idealized system: an infinite slab of mosaic crystal with thickness d, extending from $z = 0$ to $z = d$. The incoming flux $I_{\text{in}}(\hat{k})$ is assumed to originate from the region $z < 0$. Based on this configuration, the boundary conditions are defined as

$$\begin{aligned} I(\hat{k}, 0) &= I_{\text{in}}(\hat{k}) \text{ for } \hat{k}_z > 0, \\ I(\hat{k}, d) &= 0 \text{ for } \hat{k}_z < 0. \end{aligned} \tag{2.2}$$

These conditions reflect the physical assumption that neutrons enter the slab only through the bottom surface ($z = 0$), while no incoming flux present at the top boundary ($z = d$). Under this setup, the reflected and transmitted fluxes [2] are defined as

$$\begin{aligned} I_{\text{ref}}(\hat{k}) &= I(\hat{k}, 0) \text{ for } \hat{k}_z < 0, \\ I_{\text{trans}}(\hat{k}) &= I(\hat{k}, d) \text{ for } \hat{k}_z > 0. \end{aligned} \tag{2.3}$$

These definitions isolate the neutron flux reflected back from the entry surface and the flux transmitted through the slab, respectively, allowing for the analysis of how the crystal structure influences neutron propogation.

2.1.2 Bragg and Attenuation Operators

As shown in Equation 2.1, two distinct linear operators are required to represent the scattering terms in the Boltzmann equation. These are introduced as the *Bragg operator* B and the *attenuation operator* A. As previously discussed, the Bragg operator B accounts for the gain in neutron flux due to elastic scattering into a given direction, while the attenuation operator A captures the loss of flux resulting from scattering out of the current direction. Together, these operators encapsulate the redistribution of neutron intensity within the mosaic crystal due to Bragg scattering processes.

The Bragg operator B [2] is defined as follows

$$B \circ I(\hat{k}) = \int d^2\hat{k}' \mu(\hat{k}, \hat{k}') I(\hat{k}'), \tag{2.4}$$

where $d^2\hat{k}'$ denotes the differential solid angle over the integration variable $\hat{k}'$. The kernel $\mu(\hat{k}, \hat{k}')$, known as the *reflection kernel*, represents the probability density for a neutron traveling in direction $\hat{k}$ to be scattered elastically into the direction $\hat{k}'$, within an infinitesimal solid angle element around $\hat{k}'$. This kernel encapsulates the angular distribution of Bragg scattering and will be discussed in detail in Section 2.1.5.

Similar to operator B, the attenuation operator A [2] follows as

$$A(\hat{k}) = \int d^2\hat{k}' \mu(\hat{k}', \hat{k}) + \mu_a. \tag{2.5}$$

The integral term accounts for the losses by diffraction, while constant μ_a accounts for the absorption, inelastic scattering, and other losses in the system.

Both operators, B and A, depend strongly on the reflection kernel $\mu(\hat{k}', \hat{k})$, which encapsulates the scattering characteristics of the mosaic crystal. The kernel itself is determined solely by the distribution of mosaic blocks and the orientation of the crystal relative to the xy-plane, as will be shown in detail later. For the sake of simplicity, and to facilitate analytical treatment in the initial stages, we assume for now that the reflection kernel is an arbitrary function depending on $\hat{k}'$ and $\hat{k}$. This approximation allows us to focus on the structural behavior of the transport equation before incorporating the full complexity of the kernel.

2.1.3 Discretization

Now that all the essential components of the model have been introduced, the next step is to discretize the system in order to make it solvable on a numerical grid. Up to this point, the neutron flux distribution has been treated as a continuous fucntion of the propogation direction $\hat{k}$ and the spatial coordinate z. However, for numerical implementation, these continuous variables must be replaced by discrete counterparts. This involves discretizing the angular domain, as well as the spatial domain along the z-axis. Doing so transforms the differential transport equation into a finite-dimensional linear system, enabling practical computation of the flux distribution using standard numerical methods.

First, we discretize the angular domain of $\hat{k}$ into M histogram bins, indexed by $m = 1, ..., M$. Each bin corresponds to a finite solid angle $\Delta\Omega_m$ and represents the total current over that angular segment. The discretized current $I_m(z)$ [2] associated with bin m is defined as

$$I_m(z) = \int_{\Delta\Omega_m} d^2\hat{k} I(\hat{k}, z), \tag{2.6}$$

where $I(\hat{k}, z)$ is the continuous flux distribution.

To derive the discretized form of the Bragg operator B, we combine its continuous definition from Equation 2.4 with the angular discretization introduced in Equation 2.6

$$\begin{aligned}(B \circ I(z))_m &= \int_{\Delta\Omega_m} d^2\hat{k} B \circ I(\hat{k}, z) \\ &= \int_{\Delta\Omega_m} d^2\hat{k} \sum_{s=1}^{M} \int_{\Delta\Omega_s} d^2\hat{k}' \mu(\hat{k}, \hat{k}') I(\hat{k}', z) \\ &= \sum_{s=1}^{M} \int_{\Delta\Omega_m} d^2\hat{k} \mu(\hat{k}, \hat{k}') \int_{\Delta\Omega_s} d^2\hat{k}' I(\hat{k}', z).\end{aligned} \tag{2.7}$$

Here, the second integral becomes $I_s(z)$ with Equation 2.6. Moreover, we define the discrete Bragg matrix elements [2] as

$$B_{ms} = \int_{\Delta\Omega_m} d^2\hat{k} \mu(\hat{k}, \hat{k}'), \tag{2.8}$$

which transforms Bragg operator to

$$(B \circ I)_m = \sum_{s=1}^{M} B_{ms} I_s(z). \tag{2.9}$$

Starting from the discretized Bragg operator B_{ms}, we define the attenuation operator A in an analogous manner. The attenuation vector elements A_m [2] are given by

$$A_m = \int_{\Delta\Omega_m} d^2\hat{k}' \mu(\hat{k}, \hat{k}') + \mu_a \tag{2.10}$$

From this, we define the total attenuation factor A_m as the sum over all incoming angular bins

$$A_m = \sum_{s=1}^{M} B_{ms} + \mu_a. \tag{2.11}$$

This expression captures the total loss of flux from direction bin m due to both scattering into other directions and absorption.

By incorporating the discretizations from Equations 2.6, 2.9 and 2.11 into the original transport equation 2.1, we arrive at the discretized form

$$(\hat{k}_{m,z} \partial_z + A_m) I_m(z) - \sum_{s=1}^{M} B_{ms} I_s(z) = 0. \tag{2.12}$$

Having completed the angular discretization, we now proceed to discretize the spatial domain, which in our case is limited to the z-axis. For reasons that will be discussed in

Section 2.1.4, we employ Chebyshev polynomials for this discretization, which requires mapping the spatial interval $[0, d]$ to the standard Chebyshev domain $[-1, 1]$ [2]. To this end, we define a transformed coordinate

$$\zeta = -1 + \frac{2z}{d}, \tag{2.13}$$

and express the angular flux in terms of the new coordinate as

$$J_m(\zeta) = I_m(d\frac{1+\zeta}{2}). \tag{2.14}$$

Since the transport equation involves a spatial derivative, we apply the chain rule for the coordinate transformation. The derivative with respect to z transforms as

$$\partial\zeta = \frac{2}{d}\partial z. \tag{2.15}$$

Multiplying the entire equation by d to eliminate the fractional coefficient, we obtain the transformed transport equation [2]

$$(2\hat{k}_{m,z}\partial_\zeta + dA_m)J_m(\zeta) - \sum_{s=1}^{M} dB_{ms}J_s(\zeta) = 0. \tag{2.16}$$

The boundary conditions given in Equation 2.2 also transform accordingly

$$\begin{aligned} J_m(-1) &= I_{\text{in},m} \text{ for } \hat{k}_{m,z} > 0, \\ J_m(+1) &= 0 \text{ for } \hat{k}_{m,z} < 0. \end{aligned} \tag{2.17}$$

These transformed equations and boundry conditions form the basis for solving the system using spectral methods with Chebyshev polynomials in the spatial dimension.

2.1.4 Equation System

Equation 2.16 represents a system of M coupled first-order linear differential equations in the functions $J_m(\zeta)$. To solve this system, we employ the *spectral collocation* method, a high-accuracy numerical technique particularly well-suited for smooth problems. Spectral collocation approximates each unknown function $J_m(\zeta)$ with a global interpolating polynomial $P_m(\zeta)$ of degree N, which is constructed to match J_m at $N+1$ carefully chosen *collocation points* $\{\zeta_n\}$. For this purpose, we select the Chebyshev-Gauss-Lobatto points defined by

$$\zeta_n = -\cos(\frac{\pi n}{N}), \quad n = 0, 1, ..., N, \tag{2.18}$$

which are known to minimize numerical instability and yield a well-conditioned differentiation matrix [2].

The polynomial values at the collocation points are denoted as $p_{nm} = P_m(\zeta_n)$, giving rise to $M(N+1)$ unknowns in total. From the boundary conditions in Equation 2.17, M of these values are known, while the remaining ones are determined by solving the discretized transport equation 2.16. The discretized boundary conditions becomes

$$\begin{aligned} p_{0m} &= I_{\text{in},m} \text{ for } \hat{k}_{m,z} > 0, \\ p_{Nm} &= 0 \text{ for } \hat{k}_{m,z} < 0. \end{aligned} \tag{2.19}$$

To complete the discretization, we need to discretize the partial differential δ_ζ. This implementation is done through the replacement of the derivative in Equation 2.16 by the differentiation matrix D, which approximates the derivative of $P_m(\zeta)$ at the collocation points

$$\sum_{j=0}^{N} D_{nj} p_{jm} = P'_m(\zeta_n). \tag{2.20}$$

The entries of the differentiation matrix $D \in \mathbb{R}^{(N+1)\times(N+1)}$ [2] are given as follows:

- For off-diagonal entries $(i \neq j)$:

$$D_{ij} = \frac{1 + \delta_{i0} + \delta_{iN}(-1^{i+j})}{1 + \delta_{j0} + \delta_{jN}\zeta_i - \zeta_j}, \tag{2.21}$$

- For interior diagonal entries $(1 \leq j \leq N-1)$:

$$D_{jj} = -\frac{\zeta_j}{2(1-\zeta^2)}, \tag{2.22}$$

- For the endpoints:

$$D_{00} = -D_{NN} = -\frac{2N^2+1}{6}. \tag{2.23}$$

These expressions allow us to construct the differentiation matrix D, which plays a central role in translating the differential equations into a solvable algebraic system.

We now rewrite the full transport equation 2.16 in its discretized from by applying the spectral collocation approach described above. Substituting the differentiation using Equation 2.20, the transport equation becomes

$$\sum_{j=0}^{N} 2\hat{k}_{m,z} D_{nj} p_{jm} + d A_m p_{nm} - d \sum_{s=0}^{M} B_{ms} p_{ns} = 0. \tag{2.24}$$

This equation must hold for all histogram bins $m = 1, ..., M$ (i.e. angular discretization bins) and for all collocation points $n = 0, ..., N$ (i.e., spatial discretization points).

From this point onward, we will refer to elements of the discretized angular domain as *histogram bins* and elements of the discretized spatial domain as *collocation points*, to maintain a clear distinction between the two dimensions.

To further simplify the problem, all linear operators are collected into a single system matrix L [2], defined as

$$L_{nmjs} = (2\hat{k}_{mz}D_{nj} + dA_m\delta_{nj})\delta_{ms} - dB_{ms}\delta_{nj}, \text{ with } L \in \mathbb{R}^{(N+1)\times(M)}. \tag{2.25}$$

Here δ_{ij} denotes the Kronecker delta. Using this formulation, the transport equation is rewritten in compact matrix form With this transport equation is simplified to

$$\forall n = 0, ..., N \quad \forall m = 1, ..., M : \sum_{j=0}^{N}\sum_{s=1}^{M} L_{nmjs}p_{js} = 0. \tag{2.26}$$

Thanks to the Kronecker deltas in the definition and the sparsity of the Bragg matrix B_{ms}, the system matrix L is sparse. This sparsity allows for efficient and computationally inexpensive solutions.

The final step involves separating the histogram bins according to the sign of $\hat{k}_{m,z}$, since both the boundary conditions 2.2 and the quantities of interest 2.3 depend on whether the direction is incoming or outgoing [2]. Accordingly, the summation over s in Equation 2.26 is split into forward ($\hat{k}_{m,z} > 0$) and backward ($\hat{k}_{m,z} < 0$) components.

We omit the contributions from p_{Ns} for backward directions (as they are zero due to the boundary condition at $\zeta = 1$), and we shift the known terms $p_{0s} = J_{\text{in},s}$ for forward directions to the right-hand side.This yields the final system

$$\left(\sum_{j=1}^{N}\sum_{s}^{\text{forward}} + \sum_{j=0}^{N-1}\sum_{s}^{\text{backward}}\right) L_{nmjs}p_{js} = -\sum_{s}^{\text{forward}} L_{nm0s}J_{\text{in},s}. \tag{2.27}$$

This reduces the problem to a linear system of the form $Lx = y$, where the vector x contains the unknowns p_{js}, and y represents the right-hand side of Equation 2.27. The reflected and transmitted fluxes can then be extracted directly from the solution x, using the definitions provided in Equation 2.3.

2.1.5 Reflection Kernel and Distribution of Scattering Directions

Up to this point, the Bragg operator (or matrix) B and, consequently, the attenuation operator (or vector) A have been treated as arbitrary functions of the incoming and outgoing directions $\hat{k}$ and $\hat{k}'$, respectively, for the sake of simplicity. Having established

the main system of equations, we now turn to a detailed discussion of the reflection kernel $\mu(\hat{k}', \hat{k})$, which forms the foundation of both operators.

As introduced in Section 2.1.2, $\mu(\hat{k}', \hat{k})$ represents the probability density of scattering from an incoming direction $\hat{k}$ into an infinitesimal solid angle $d^2\hat{k}'$ around the outgoing direction $\hat{k}'$ [2]. The kernel can be expressed as a sum over single-reflection transfer functions associated with different lattice planes

$$\mu(\hat{k}', \hat{k}) = \sum_{hkl} \mu_{hkl}(\hat{k}', \hat{k}), \tag{2.28}$$

where the single-reflection transfer function $\mu_{hkl}(\hat{k}', \hat{k})$ [2] is defined by

$$\mu_{hkl}(\hat{k}', \hat{k}) = \int d^2\hat{G} W_{hkl}(\hat{G}) \mu_{hkl}^{\text{block}}(\hat{k}', \hat{k}, \hat{G}). \tag{2.29}$$

Here μ_{hkl}^{block} denotes the block transfer function, and $W_{hkl}(\hat{G})$ is the statistical distribution of scattering directions $\hat{G}$ within a single crystalline block. We will define both μ_{hkl}^{block} and $W_{hkl}(\hat{G})$ in the following.

For simplification, we consider only one pair of reflections, hkl and its inverse $\bar{h}\bar{k}\bar{l}$, and assume identical block transfer functions for both. These reflections share a combined scattering distribution

$$W(\hat{G}) = W_{hkl}(\hat{G}) + W_{\bar{h}\bar{k}\bar{l}}(\hat{G}). \tag{2.30}$$

Substituting Equation 2.29 into Equation 2.28 yields

$$\mu(\hat{k}', \hat{k}) = \int d^2\hat{G} W(\hat{G}) \mu_{\text{block}}(\hat{k}', \hat{k}, \hat{G}). \tag{2.31}$$

Returning to the definition of the block transfer function μ_{hkl}^{block}, we use a definition derived in [17, 2] and given by

$$\mu_{hkl}^{\text{block}}(\hat{k}', \hat{k}, \hat{G}) = \bar{\mu} \cos\theta_B \delta(\hat{k} \cdot \hat{G} - \sin\theta_B) \delta^2(\hat{k}' - \hat{k} + 2\sin\theta_B \hat{G}), \tag{2.32}$$

where θ_B is the Bragg angle, and prefactor $\bar{\mu}$ is defined as

$$\bar{\mu} = \frac{(2\pi)^3 |F_{hkl}|^2}{2V^2 k^3 \cos\theta_B \sin\theta_B}, \tag{2.33}$$

where F_{hkl} is the structure factor, V is the unit cell volume and k is the wavenumber. Two important remarks follow from this expression: First, since the block transfer function depends on $|F_{hkl}|^2$, it is identical for both reflections hkl and $\bar{h}\bar{k}\bar{l}$, consistent with the earlier assumption. Because of that, the block transfer function is now denoted as μ_{block} as it written in Equation 2.31. Second, the Bragg angle θ_B is treated as a constant

throughout the system, independent of the particular reflection, as we consider a fixed reflection *hkl* and a constant wavenumber k.

To evaluate the integral in Equation 2.31, we first consider the action of the integration over $\hat{G}$ on the first delta function in Equation 2.32 [2]. We parametrize $\hat{G}$ in spherical coordinates (θ, t) with respect to the axis $\hat{k}$, and introduce a generic test function $f(\hat{G})$. This gives

$$\int d^2\hat{G}\delta(\hat{k}\hat{G} - \sin\theta_B) f(\hat{G}) = \int_{-\frac{\pi}{2}}^{\frac{\pi}{2}} d\theta \cos\theta \int_0^{2\pi} dt (\sin\theta - \sin\theta_B) f(\hat{G}(\theta, t)), \tag{2.34}$$

which, due to the delta function reduces to

$$\int_0^{2\pi} dt f(\hat{G}(\theta_B, t)). \tag{2.35}$$

Geometrically, this integration corresponds to a complete rotation in t around the circle defined by the intersection of the unit sphere with the Bragg plane

$$\hat{G} \cdot \hat{k} = \sin\theta_B, \tag{2.36}$$

as already implied by the first delta function in Equation 2.32.

We now replace the test function $f(\hat{G}(\theta, t))$ with $W(\hat{G})\delta^2(\hat{k}' - \hat{k} + 2\sin\theta_B \cdot \hat{G})$, and include the prefactor $\bar{\mu}\cos\theta_B$ from Equation 2.31. This yields

$$\mu(\hat{k}', \hat{k}) = \bar{\mu}\cos\theta_B \int_0^{2\pi} dt W(\hat{G})\delta^2(\hat{k}' - \hat{k} + 2\sin\theta_B \cdot \hat{G}). \tag{2.37}$$

In this expression, the delta function enforces the kinematic constraint that the outgoing direction $\hat{k}'$ must satisfy

$$\hat{k}' = \hat{k} - 2\sin\theta_B \cdot \hat{G}, \tag{2.38}$$

which we refer to as the *deflection function* [2]

$$\hat{\kappa} = \hat{k} - 2\sin\theta_B \cdot \hat{G}. \tag{2.39}$$

Since the integration variable is t, we must provide an explicit parametrization of $\hat{G}$ in terms of t to proceed.

Because of that now we enforce a parametric curve $\hat{G} = \hat{\Gamma}(\hat{k}, t)$ with $t \in [0, 2\pi)$. To construct this curve, we begin by selecting an orhonormal basis $\hat{e}_x, \hat{e}_y, \hat{e}_z$ for representing the reciprocal-space vectors $\hat{k}$ and $\hat{G}$ [2]. In the present model, the crystal normal $\hat{z}$ is identified with the basis vector $\hat{e}_z$. The incoming beam direction $\hat{k}$ is then defined via successive rotations using the rotation matrices $R_y(\alpha)$ and $R_z(\beta)$, which correspond to the spherical coordinate angles θ and ϕ, respectively, in the Cartesian coordinate system.

The rotation matrices are given by

$$R_y(\alpha) = \begin{pmatrix} \cos\alpha & 0 & \sin\alpha \\ 0 & 1 & 0 \\ -\sin\alpha & 0 & \cos\alpha \end{pmatrix}, \quad R_z(\beta) = \begin{pmatrix} \cos\beta & -\sin\beta & 0 \\ \sin\beta & \cos\beta & 0 \\ 0 & 0 & 1 \end{pmatrix}. \tag{2.40}$$

In our formulation, the rotation applied to the incident wavevector $\hat{k}$ is constructed as the successive application

$$R_k = R_z(\phi_{\hat{k}}) R_y(\frac{\pi}{2} - \theta_{\hat{k}}), \tag{2.41}$$

where the polar angle $\theta_{\hat{k}}$ is defined as the angle between the vector $\hat{k}$ and the unit vector $\hat{e}_z$. The parameter α corresponds to the angle between $\hat{e}_y$ and $\hat{k}$, which is equal to $\frac{\pi}{2} - \theta_{\hat{k}}$. Consequently, by applying the corresponding trigonometric identities, the rotation matrix around the y-axis takes the form

$$R_y(\frac{\pi}{2} - \theta_{\hat{k}}) = \begin{pmatrix} \sin\theta_{\hat{k}} & 0 & \cos\theta_{\hat{k}} \\ 0 & 1 & 0 \\ -\cos\theta_{\hat{k}} & 0 & \sin\theta_{\hat{k}} \end{pmatrix} \tag{2.42}$$

This rotation maps the reciprocal vector $\hat{k}$ onto

$$\hat{k} = R_k \hat{e}_z = \begin{pmatrix} \cos\theta_{\hat{k}} \cos\phi_{\hat{k}} \\ \cos\theta_{\hat{k}} \sin\phi_{\hat{k}} \\ \sin\theta_{\hat{k}} \end{pmatrix}. \tag{2.43}$$

From this definition, we can now introduce a parametric curve, dependent on $\hat{e}_z$ and a parameter t, which satisfies the Laue-Bragg condition in Equation 2.36

$$\hat{\Gamma}(\hat{e}_z, t) = \begin{pmatrix} \cos\theta_B \cos t \\ \cos\theta_B \sin t \\ \sin\theta_B \end{pmatrix}, \tag{2.44}$$

which geometrically describes a circle representing all possible scattering directions $\hat{G}$.

To obtain $\hat{\Gamma}(\hat{k}, t)$, we perform a rotation using the same rotation matrix R_k. In this case, the rotation around the z-axis can be omitted because t (the azimuthal angle ϕ) appears only within a full-period integral in Equation 2.37, and any shift in t does not affect the integral. Exploiting this property, the full parametric curve becomes

$$\begin{aligned} \hat{\Gamma}(\hat{k}, t) = R_y(\frac{\pi}{2} - \theta_{\hat{k}}) \hat{\Gamma}(\hat{e}_z, t) &= \begin{pmatrix} \cos\theta_B \sin\theta_{\hat{k}} \cos t + \sin\theta_B \cos\theta_{\hat{k}} \\ \cos\theta_B \sin t \\ -\cos\theta_B \cos\theta_{\hat{k}} \cos t + \sin\theta_B \sin\theta_{\hat{k}} \end{pmatrix} \\ &= \begin{pmatrix} \alpha(\theta_{\hat{k}}, t) \\ \beta(t) \\ \gamma(\theta_{\hat{k}}, t) \end{pmatrix}, \end{aligned} \tag{2.45}$$

where we introduce the scalar functions α, β, γ to simplify the notation [2]. This parametrization can now be applied to the deflection function $\hat{\kappa}$ in Equation 2.39. We insert the parametric curve $\hat{\Gamma}(\hat{k}, t)$ in Equation 2.39, yielding

$$\begin{aligned} \hat{\kappa} &= \hat{k} - 2\sin\theta_B \cdot \hat{\Gamma}(\hat{k}, t) \\ &= R_k[\hat{e}_z - 2\sin\theta_B \hat{\Gamma}(\hat{e}_z, t)]. \end{aligned} \tag{2.46}$$

Defining $\hat{\kappa}(\hat{e}_z, t) = \hat{e}_z - 2\sin\theta_B \hat{\Gamma}(\hat{e}_z, t)$, we have

$$\hat{\kappa}(\hat{k}, t) = R_k \hat{\kappa}(\hat{e}_z, t) = R_z(\phi_{\hat{k}}) R_y(\frac{\pi}{2} - \theta_{\hat{k}}) \hat{\kappa}(\hat{e}_z, t). \tag{2.47}$$

After applying the rotation around y-axis, the deflection function becomes

$$\hat{\kappa}(\hat{k}, t) = R_z(\phi_{\hat{k}}) \begin{pmatrix} \cos\theta_{\hat{k}} - 2\sin\theta_B \alpha(\theta_{\hat{k}}, t) \\ 0 - 2\sin\theta_B \beta(t) \\ \sin\theta_{\hat{k}} - 2\sin\theta_B \gamma(\theta_{\hat{k}}, t) \end{pmatrix}. \tag{2.48}$$

Following the derivation in [2], this can be expressed in spherical coordinates as

$$\hat{\kappa}(\hat{k}, t) = R_z(\phi_{\hat{k}}) \begin{pmatrix} \cos\Theta(\theta_{\hat{k}}, t)\cos\Delta\Phi(\theta_{\hat{k}}, t) \\ \cos\Theta(\theta_{\hat{k}}, t)\sin\Delta\Phi(\theta_{\hat{k}}, t) \\ \sin\Theta(\theta_{\hat{k}}, t) \end{pmatrix}, \tag{2.49}$$

where the polar deflection function $\Theta(\theta, t)$ [2] and azimuthal shift function $\Delta\Phi(\theta, t)$ [2] are introduced as

$$\begin{aligned} \Theta(\theta, t) &= \arcsin(\sin\theta - 2\sin\theta_B \gamma(\theta, t)), \\ \Delta\Phi(\theta, t) &= \arctan(\frac{-2\sin\theta_B \beta(t)}{\cos\theta - 2\sin\theta_B \alpha(\theta, t)}). \end{aligned} \tag{2.50}$$

Since the rotation around z is trivial in spherical coordinates, the complete deflection function can be written as

$$\hat{\kappa}(\theta_{\hat{k}}, t) = \begin{pmatrix} \Theta(\theta_{\hat{k}}, t) \\ \phi_{\hat{k}} + \Delta\Phi(\theta_{\hat{k}}, t) \end{pmatrix} = \begin{pmatrix} \theta_{\hat{\kappa}} \\ \phi_{\hat{\kappa}} \end{pmatrix}. \tag{2.51}$$

With this expressions, the block transfer function (Equation 2.37) takes the form

$$\mu(\hat{k}', \hat{k}) = \bar{\mu}\cos\theta_B \int_0^{2\pi} dt W(\hat{\Gamma}(\hat{k}, t)) \delta^2(\hat{k}' - \hat{\kappa}(\hat{k}, t)). \tag{2.52}$$

The final component needed for the reflection kernel is the block orientation distribution $W(\hat{G})$ (or $W(\hat{\Gamma}(\hat{k}, t))$). For mosaic crystals, W is usually the same in all directions

around the crystal normal $\hat{H}$, so it only depends on the angle between $\hat{G}$ and $\hat{H}$ [2]. In this study, we focus on the $00l$ reflections, where the scattering occurs along the direction of the block normals. Therefore, $W(\hat{G})$ can be approximated by a disc-like distribution, which we model using the Mises-Fisher (MF) distribution [2]

$$W_{\pm(hkl)}(\hat{G}) = \frac{1}{2\pi\eta^2(1-\exp(\frac{-2}{\eta^2}))}\exp(-\frac{(\hat{G}\mp\hat{H})^2}{2\eta^2}), \tag{2.53}$$

where η is the standard deviation. Defining $A = \frac{1}{2\pi\eta^2(1-\exp(\frac{-2}{\eta^2}))}$ and inserting the previous definition to Equation 2.30, we have

$$W(\hat{G}) = A\cdot[\exp(\frac{-\hat{G}^2-\hat{H}^2+2|\hat{G}\cdot\hat{H}|}{2\eta^2}) + \exp(\frac{-\hat{G}^2-\hat{H}^2-2|\hat{G}\cdot\hat{H}|}{2\eta^2})]. \tag{2.54}$$

Since $\hat{G}$ and $\hat{H}$ are normalized ($\hat{G}^2 = \hat{H}^2 = 1$), this simplifies to

$$W(\hat{G}) = A\cdot\exp(-\frac{1}{\eta^2})[\exp(\frac{|\hat{G}\cdot\hat{H}|}{\eta^2}) + \exp(-\frac{|\hat{G}\cdot\hat{H}|}{\eta^2})]. \tag{2.55}$$

Neglecting the second term as we assume the overlap between W_{hkl} and $W_{\bar{h}\bar{k}\bar{l}}$ is negligible, the distribution can be approximated as

$$W(\hat{G}) \approx A\cdot\exp(\frac{-1+|\hat{G}\cdot\hat{H}|}{\eta^2}). \tag{2.56}$$

For a normal-oriented mosaic ($\hat{H} = \hat{e}_z$), the distribution depends solely on $\gamma(\theta_{\hat{k}}, t)$, since contributions from other terms vanish in the scalar product. This results with the following approximation

$$W(\hat{G}) \approx A\cdot\exp(\frac{-1+\gamma(\theta_{\hat{k}},t)}{\eta^2}). \tag{2.57}$$

With this approximation, Equation 2.52 takes the form

$$\mu(\hat{k}',\hat{k}) = A\bar{\mu}\cos\theta_B\int_0^{2\pi} dt\exp(\frac{-1+\gamma(\theta_{\hat{k}},t)}{\eta^2})\delta^2(\hat{k}'-\hat{\kappa}(\hat{k},t)). \tag{2.58}$$

From this formulation of the reflection kernel, the Bragg matrix B can be constructed, and consequently the attenuation vector A is obtained. The detailed procedure for this construction is provided in Section 3.2.3.

2.1.6 Material Parameters

In order to construct a reliable numerical model for the crystals under investigation, it is necessary to introduce suitable material parameters. The first of these is the Bragg angle θ_B, which was previously defined as a fundamental characteristic of the system. Throughout the computations, θ_B is treated as a constant, since both the reflection condition and the wavenumber is fixed. Owing to its central role, it is explicitly retained as an independent parameter.

To further reduce the number of variables in the model, two additional dimensionless parameters are introduced. These parameters were originally introduced and derived in [17] and [2]. For completeness, their definitions are restated here without repeating the derivations.

The first parameter is the opacity τ, defined as

$$\tau = \frac{d}{\sin\theta_B}[\bar{\mu}\mathcal{G}(0) + \mu_a], \tag{2.59}$$

where d is the crystal thickness, and $\mathcal{G}(0) = \frac{1}{\sqrt{2\pi}\eta}$. The factor $\mathcal{G}(0)$ corresponds to the central value of the prefactor of the von Mises-Fisher distribution in Equation 2.53, apart from the normalization factor $(1 - \exp(\frac{-2}{\eta^2}))$. Physically, the opacity quantifies the effective thickness of the crystal, incorporating both scattering and absorption effects: a larger τ corresponds to thicker crystal and stronger attenuation of the transmitted beam.

The second dimensionless parameter is the relative reflectivity ρ, defined as

$$\rho = \frac{\bar{\mu}\mathcal{G}(0)}{\bar{\mu}\mathcal{G}(0) + \mu_a}. \tag{2.60}$$

The ratio characterizes the balance between coherent reflection and absorption. A higher value of ρ indicates that reflection dominates over absorption.

For later convenience, these definitions can be inverted to express the effective coefficients $\bar{\mu}$ and μ_a in terms of τ and ρ as

$$\begin{aligned} d\bar{\mu} &= \sin\theta_B \frac{\rho\tau}{\mathcal{G}(0)} \\ d\mu_a &= \sin\theta_B(1-\rho)\tau. \end{aligned} \tag{2.61}$$

The advantage of this formulation is that neither $\bar{\mu}$ nor μ_a are fixed material constants; both depend on the wavelength and can therefore be adjusted. By expressing the system in terms of the dimensionless parameters τ and ρ, one can assign them arbitrary values and directly compare different cases without explicitly specifying additional material parameters.

As an illustrative example, consider two crystals of identical compositon but different thickness. If the thinner crystal is assigned $\tau = 1$, then the opacity of a crystal with double the thickness would be $\tau = 2$, while ρ remains unchanged. This parametrization therefore provides a compact and flexible framework for analyzing the influence of geometry and absorption on reflectivity.

2.2 Reflection Model for a Stack of Tilted Mosaic Crystals

Up to this point, we have established the numerical model for a single thick mosaic crystal, following the theoretical framework outlined in [2]. Building on this foundation, we now extend the model to describe a stack of normally oriented crystals, guided in part by the approach discussed in [18]. Subsequently, we introduce the effect of crystal tilting, incorporating the formulation developed in Section 2.1.5. Although this study is motivated by the PST chopper of a third-generation neutron backscattering spectrometer, we begin with the general case of a stack of $\mathcal{N}_{\text{tot}}$ crystals. The subsequent implementation, however, will be carried out explicitly for $\mathcal{N} = 3$.

2.2.1 Stack of Normal Oriented Mosaic Crystals

We consider a system consisting of three back-to-back crystals with identical orientation, $\hat{H}_0 = \hat{e}_z$. Each crystal is characterized by the same Bragg matrix B and attenuation factor A, such that the crystals are equivalent.

Compared with the single-crystal case, the most significant modification lies in the implementation of the spectral collocation method. Previously, a coordinate transformation was applied to the depth coordinate z, as defined in Equations 2.13,2.14,2.15, leading to the discretized form given in Equation 2.16. For multi-crystal case, however, it is necessary to establish an approach that is both suitable for extended geometry and consistent with the single-crystal framework.

A conceivable approach would be to treat the entrie stack as a single effective crystal, such that the system is formally identical to the single-crystal case, while allowing the matrices B and A to vary depending on the depth coordinate z. However, this method encounters serious limitations due to the choice of collocation points (Equation 2.18). In particular , an equal distribution of collocation points across each region is not achievable, and the boundary conditions at the interfaces are not properly enforced.

This issue is illustrated in Figure 2.1, where a total of 50 collocation points distributed over three regions of equal length results in the central region being populated with fewer points, while the boundaries remain unrepresented. Such an unequal distribution can lead to numerical inaccuracies, and the lack of collocation points at the boundaries

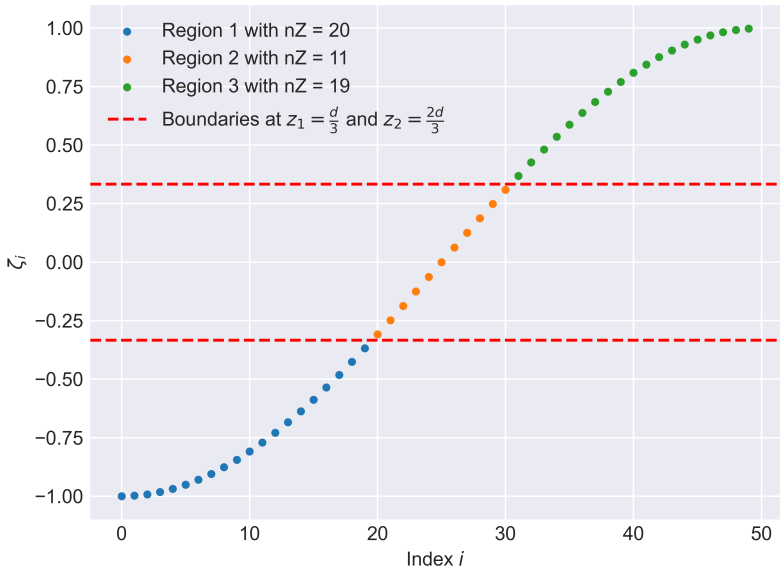

Figure 2.1: Distribution of 50 collocation points across three regions. Collocation points in different regions are indicated by distinct colors, while the red horizontal lines mark the interior boundaries between the regions. The number of collocation points assigned to each region is specified in the legend. Notably, no collocation points coincide with the boundary positions.

directly violates the imposed boundary conditions. For these reasons, this approach is deemed unsuitable and is therefore avoided.

Taking inspiration from [18], we adopt an inverse approach. Rather than dividing the single-crystal model into separate regions, we treat the system as consisting of $\mathcal{N}_{\text{tot}}$ coupled single-crystal models, connected through interior periodic boundary conditions. To extend the model in this manner, the indices of the original formulation must first be redefined so that the single-crystal description can be consistently adapted to the stack model.

The first assumption underlying this approach is that each crystal in the stack has an effective thickness of $\frac{d}{\mathcal{N}_{\text{tot}}}$. Based on this assumption, we introduce an extended transformation for the angular flux, analogous to Equation 2.14,

$$J_m^{\mathcal{N}}(\zeta) = I_m\left(\left[\mathcal{N} + \frac{1+\zeta}{2}\right] \cdot \frac{d}{\mathcal{N}_{\text{tot}}}\right), \tag{2.62}$$

where $\mathcal{N} = 0, 1, 2, ..., \mathcal{N}_{\text{tot}} - 1$ denotes the crystal index. This formulation enables the angular flux histograms to be represented separately for each crystal region.

As in the single-crystal case, the spectral collocation method is then employed to approximate the functions $J_m^{\mathcal{N}}(\zeta)$ with polynomials $P_m^{\mathcal{N}}(\zeta)$. To avoid ambiguity, we introduce a global notation,

$$y_{pm} = P_m^{\mathcal{N}}(\zeta_n), \tag{2.63}$$

where $p = 0, 1, 2, ..., (\mathcal{N} \cdot N)$ is the global index of spatial discretization across the entire system, while m and n denote the previously introduced angular and spatial discretization indices, respectively. The index n now becomes a local spatial index within each crystal. The points ζ_i correspond to the extrema of Chebyshev polynomials, as defined in Equation 2.18.

The interior boundary conditions between adjacent regions can now be expressed as

$$P_m^{\mathcal{N}}(+1) = P_m^{\mathcal{N}+1}(-1) \quad \Leftrightarrow \quad y_{p,m} = y_{p+1,m} \quad \text{for} \quad p \bmod \mathcal{N} \cdot N = 0, \tag{2.64}$$

where the modulo operator ensures the correct selection of boundary indices. The main boundary conditions from Equation 2.19 are correspondingly extended as

$$\begin{aligned} y_{0m} &= I_{\text{in},m} \text{ for } \hat{k}_{m,z} > 0, \\ y_{(\mathcal{N}_{\text{tot}} \cdot N),m} &= 0 \text{ for } \hat{k}_{m,z} < 0. \end{aligned} \tag{2.65}$$

With these boundary conditions in place, we can formulate the system of equations for the stack model in analogy with Equation 2.24. Since the number of collocation points is identical in each crystal, the differentiation matrix D_{nj} is the same for all subregions. The only differences arise from the Bragg matrix B and the attenuation factor A. Although we assume here that B and A are identical for all crystals, they are nevertheless indexed to allow for generalization.

For a single crystal within the stack, Equation 2.24 is therefore rewritten as

$$\sum_{j=0}^{N} 2\hat{k}_{m,z} D_{nj} y_{pm} + d A_m^{\mathcal{N}} y_{pm} - d \sum_{s=0}^{M} B_{ms}^{\mathcal{N}} y_{ps} = 0, \tag{2.66}$$

where the relation $p = \mathcal{N} \cdot N + n$ connects the global index p to the local spatial index n. As in Equations 2.25 and 2.26, we now define the matrix L for a single crystal as

$$L_{nmjs}^{\mathcal{N}} = (2\hat{k}_{mz} D_{nj} + d A_m^{\mathcal{N}} \delta_{nj}) \delta_{ms} - d B_{ms}^{\mathcal{N}} \delta_{nj}, \tag{2.67}$$

which differs from the single-crystal case only by the inclusion of the indices for B and A. Finally, the full equation system for the stack model can be written in analogy with Equation 2.26 as

$$\forall \mathcal{N} = 0, ..., \mathcal{N}_{\text{tot}} - 1; \quad \forall n = 0, ..., N; \quad \forall m = 1, ..., M : \sum_{j=0}^{N} \sum_{s=1}^{M} L_{nmjs}^{\mathcal{N}} y_{ps} = 0. \tag{2.68}$$

This formulation ensures that ech crystal in the stack is modeled in complete analogy to the single-crystal case, while simultaneously maintaining consistency across the entire system.

To proceed, we must now introduce the boundary conditions. In the single-crystal case, the main boundary conditions were formulated in 2.27. There, the histogram bins were separated into forward- and backward-propogating components, such that the vanishing terms in p_{Ns} were discarded, and the nonzero terms in p_{0s} were shifted to the right-hand side of the equation.

In the stack case, this procedure still guarantees the validity of the main boundary conditions given in Equation 2.65. However, in addition, the presence of multiple interfaces between crystals requires the introduction of the interior boundary conditions, which provide continuity of the solution across neighboring regions. From this point onward, we will refer the ability to enforce continuity between adjacent regions as *reflection-coupling* or *transmission-coupling*, depending on the propogation direction.

To solve the stack model, we construct the complete system of equations. For clarity, we illustrate the case with $\mathcal{N}_{\text{tot}} = 3$. In matrix form, using Equation 2.68, the system can be written as

$$\begin{pmatrix} L^0 & 0 & 0 \\ 0 & L^1 & 0 \\ 0 & 0 & L^2 \end{pmatrix} \begin{pmatrix} y^0 \\ y^1 \\ y^2 \end{pmatrix} = \begin{pmatrix} 0 \\ 0 \\ 0 \end{pmatrix}, \tag{2.69}$$

where, for readibility, we have omitted the full subscripts in the matrices L_{nmjs} and y_{ps}, while superscripts denote to which crystal they belong.

In order to incorporate boundary conditions into the system, two key modifications are introduced.

First, the boundary conditions are implemented directly in the matrix formulation in a simplified bur systematic manner. To achieve this, two additional rows are appended to the expanded matrix L, accompanied by two new unknowns at the end of the vector y, and two zeros appended to the null vector. These additional rows correspond to *coupling operators*, denoted as I^1 and I^2.

As an example, for the first boundary condition, the operators are defined as $1 \times M$ vectors with entries

$$I_p^1 = \begin{cases} 1, & \text{for} \quad p = N-1 \vee p = \mathcal{N} \cdot N - 2 \\ 0, & \text{otherwise} \end{cases}, \quad I_p^2 = \begin{cases} 1, & \text{for} \quad p = N \vee p = \mathcal{N} \cdot N - 1 \\ 0, & \text{otherwise} \end{cases}, \tag{2.70}$$

where the index conditions depend on the specific boundary condition being applied.

The introduction of the additional conditions ensures that the diagonal structure of the full matrix L is preserved, preventing the occurrence of empty columns that would otherwise result in a zero determinant. The inclusion of two zeros at the end of the

null vector guarantees that the boundary conditions take the form $y^0_{N-1} = y^1_0$. The new entries at the end of the vector y can be interpreted as *coupling strenghts*, since in the complete equation form the last two equations are given by

$$\begin{aligned} \lambda^1(y^0_{N-1} - y^1_0) &= 0, \\ \lambda^2(y^1_{N-1} - y^2_0) &= 0. \end{aligned} \tag{2.71}$$

For the moment, the auxiliary unknowns λ^1 and λ^2 can be omitted. This straightforward implementation provides a consistent enforcement of the boundary conditions defined in Equation 2.65.

In its complete form, for the system matrix $\mathcal{N}_{\text{tot}} = 3$ takes the block-structured form

$$\begin{pmatrix} L^0 & 0 & 0 & 0 & 0 \\ 0 & L^1 & 0 & 0 & 0 \\ 0 & 0 & L^2 & 0 & 0 \\ I^1 & -I^2 & 0 & 1 & 0 \\ 0 & I^1 & -I^2 & 0 & 1 \end{pmatrix} \begin{pmatrix} y^0 \\ y^1 \\ y^2 \\ \lambda^1 \\ \lambda^2 \end{pmatrix} = \begin{pmatrix} 0 \\ 0 \\ 0 \\ 0 \\ 0 \end{pmatrix}. \tag{2.72}$$

This formulation incorporates the boundary equations while maintaining the square structure of the total matrix and ensuring a non-vanishing determinant.

Second, the right-hand side of the system must be constructed in analogy with Equation 2.27, where the forward and backward propogating channels are separated in order to correctly enforce flux continuity across regions. For each crystal, the corresponding equation is reconstructed as

$$\left(\sum_{j=1}^{N} \sum_{s}^{\text{forward}} + \sum_{j=0}^{N-1} \sum_{s}^{\text{backward}} \right) L^{\mathcal{N}}_{nmjs} y^{\mathcal{N}}_{js} = - \sum_{s}^{\text{forward}} L^{\mathcal{N}}_{nm0s} y_{p,s}, \tag{2.73}$$

where the index $p = 0, N, 2N$ denotes the first collocation point of each crystal, hence y_{ps} becomes the incoming flux $J_{\text{in},s}$ for each crystal in the system.

In the single-crystal case, the right-hand side of Equation 2.27 already incorporates the boundary conditions of Equation 2.2. There, the first boundary condition is explicitly present, while the second is trivial since it assumes zero reflection at the crystal boundary. This assumption, however, does not hold for the stack case. At each internal boundary, a backward-propogating contribution arises from the adjacent crystal. Since these terms were absent in the single-crystal case, a new formulation is required to consistently describe the reflection coupling between neighboring regions.

Moreover, this raises follow-up considerations regarding transmission coupling as well. While the external boundary conditions can be directly set by the incoming beam, as shown in Equation 2.65, the central challenge lies in defining the interior

boundary conditions: how should the forward- and backward-propogating components be coupled across the interfaces between regions?

For the transmission coupling, we adopt a simplifying assumption. Specifically, the incoming beam at the first crystal is treated as if it were propogating through a single crystal with identical properties. In other words, the transmitted beam at the first interior boundary is taken to be equal to the transmitted beam of an isolatad crystal. This assumption is then applied successively at each crystal interface in the system.

The limitation of this approach lies in the neglect of possible re-reflections at the internal interfaces. These re-reflected components could, in principle, contribute to the forward-propogating distribution. However, for the present treatment we assume that their effect is negligible and falls within the margin of the numerical deviations already inherent to the computation.

The implementation of the forward-propogating boundary conditions is performed using a reference system: an identical incoming beam is sent to a single crystal, and its transmitted distribution is extracted. This distribution is then employed in the stack model to represent the forward transmission at each subsequent interface.

In contrast, the formulation of the reflection coupling is not yet fully developed, as a rigorous derivation is still required. For the moment, while the explicit reflected beam cannot be obtained within the current scheme, the total reflection can nonetheless be determined in directly. This is achieved through the relation between transmission and reflection, assuming no absorption in the system, i.e. $\rho = 1$ (equivalently, μ_a=0), while accounting for numerical deviations.

A natural extension of the present formalism would be the incorporation of reflection coupling, which can be initiated based on the framework already established in Equation 2.27. In addition to the separation of the incoming beam at the first collocatiopn point of the crystal, one may also extract the reflected beam in an analogous manner. This modification leads to an expansion of the current interface formulation, which can be expressed as

$$\left(\sum_{j=1}^{N}\sum_{s}^{\text{forward}} + \sum_{j=0}^{N-1}\sum_{s}^{\text{backward}}\right) L^{\mathcal{N}}_{nmjs} y^{\mathcal{N}}_{js} = -\sum_{s}^{\text{forward}} L^{\mathcal{N}}_{nm0s} y_{p,s} - \sum_{s}^{\text{backward}} L^{\mathcal{N}+1}_{nm0s} J^{\mathcal{N}+1}_{\text{ref},s}, \quad (2.74)$$

where $J^{\mathcal{N}+1}_{\text{ref},s}$ denotes the outgoing flux reflected from the crystal $\mathcal{N}+1$.

This formulation provides a consistent starting point for defining reflection coupling through the explicit treatment of the interior boundary conditions. By embedding the reflected contributions within the interface relations, one obtains a more complete description of multi-layer scattering, which in turn lays the groundwork for future implementations of a fully coupled forward- and backward-propogating beam formalism.

2.2.2 Tilted Crystal Formulation

Finally, we will introduce a reformulation for the tilted crystals with respect to the original crystal normal $\hat{H}_0 = \hat{e}_z$. Tilting of the crystals in the general model only effects the Bragg matrix B and attenuation vector A depending on in which depth coordinate z the beam is travelling. This means the only needed modification to extend the model for a stack of tilted crystal is to redefine the matrix B and vector A for each region differently, which will change the matrix $L^{\mathcal{N}}$ depending on how deep the beam is.

We begin by redefining the crystal normals in the presence of a tilt. Introducing a tilt to the crystal modifies the crystal normal $\hat{H}$. To account for this effect, we define the tilting angle χ as a rotation around the y-axis. Consequently, the crystal normal transforms as

$$\hat{H}' = R_y(\chi)\hat{H}_0 = R_y(\chi)\hat{e}_z = \begin{pmatrix} \cos\chi & 0 & \sin\chi \\ 0 & 1 & 0 \\ -\sin\chi & 0 & \cos\chi \end{pmatrix} \begin{pmatrix} 0 \\ 0 \\ 1 \end{pmatrix} = \begin{pmatrix} \sin\chi \\ 0 \\ \cos\chi \end{pmatrix}. \tag{2.75}$$

This transformation is applied both to the parametric curve $\Gamma(\hat{k}, t)$ and the deflection function $\hat{\kappa}(\hat{k}, t)$. For the parametric curve defined in Equation 2.45, which is expressed in terms of scalar functions $\alpha(\theta, t)$, $\beta(t)$ and $\gamma(\theta, t)$, together with the rotation matrix around the y-axis given in Equation 2.40, the transformation expression reads

$$\hat{\Gamma}'(\hat{k}, t) = R_y(\chi)\hat{\Gamma}(\hat{k}, t) = \begin{pmatrix} \cos\chi \cdot \alpha(\theta, t) + \sin\chi \cdot \gamma((\theta, t)) \\ \beta(t) \\ \cos\chi \cdot \gamma(\theta, t) - \sin\chi \cdot \alpha((\theta, t)) \end{pmatrix}. \tag{2.76}$$

Analogously, the deflection function transforms as

$$\hat{\kappa}'(\hat{k}, t) = R_y(\chi)\hat{\kappa}(\hat{k}, t) = \begin{pmatrix} \cos(\theta - \chi) - 2\sin\theta_B(\cos\chi \cdot \alpha(\theta, t) + \sin\chi \cdot \gamma(\theta, t)) \\ -2\sin\theta_B\beta(t) \\ \sin(\theta - \chi) - 2\sin\theta_B(\cos\chi \cdot \gamma(\theta, t) - \sin\chi \cdot \alpha(\theta, t)) \end{pmatrix}, \tag{2.77}$$

where the trigonometric identities $\cos\chi \cdot \sin\theta - \sin\chi \cdot \cos\theta = \sin(\theta - \chi)$ and $\cos\chi \cdot \cos\theta + \sin\chi \cdot \sin\theta = \cos(\theta - \chi)$ were used. The polar deflection function $\Theta(\theta, t)$ and the azimuthal shift function $\Delta\Phi(\theta, t)$, defined in Equation 2.49, then transform as

$$\begin{aligned} \Theta'(\theta, t) &= \arcsin(\sin(\theta - \chi) - 2\sin\theta_B(\cos\chi \cdot \gamma(\theta, t) - \sin\chi \cdot \alpha(\theta, t))), \\ \Delta\Phi'(\theta, t) &= \arctan\left(\frac{-2\sin\theta_B \cdot \beta(t)}{\cos(\theta - \chi) - 2\sin\theta_B(\cos\chi \cdot \alpha(\theta, t) + \sin\chi \cdot \gamma(\theta, t))}\right). \end{aligned} \tag{2.78}$$

This construction ensures that the incoming angle θ remains invariant, thereby preserving angular consistency across the discretization grid, particularly important in

the case of stacked crystals. Maintaining this consistency prevents unphysical scattering outside the angular domain and reduces numerical errors.

Next, we verify whether the von Mises-Fisher distribution in Equation 2.57 remains valid for tilted crystals. Since the scalar product is invariant under rotations, i.e $\hat{G}' \cdot \hat{H}' = \hat{G} \cdot \hat{H}$, the distribution should remain unaffected. Explicitly,

$$\begin{aligned}\hat{G}' \cdot \hat{H}' &= \begin{pmatrix} \cos\chi \cdot \alpha(\theta,t) + \sin\chi \cdot \gamma(\theta,t) \\ \beta(t) \\ \cos\chi \cdot \gamma(\theta,t) - \sin\chi \cdot \alpha(\theta,t) \end{pmatrix} \cdot \begin{pmatrix} \sin\chi \\ 0 \\ \cos\chi, \end{pmatrix} \\ &= \sin\chi \cdot \cos\chi \cdot \alpha(\theta,t) + \sin^2\chi \cdot \gamma(\theta,t) + \cos^2\chi \cdot \gamma(\theta,t) - \cos\chi \cdot \sin\chi \cdot \alpha(\theta,t), \\ &= \gamma(\theta,t) = \hat{G} \cdot \hat{H}, \end{aligned} \tag{2.79}$$

thereby confirming that no modification of $W(\hat{\Gamma}(\hat{k},t))$ is required. With the transformed functions $\Theta(\theta,t)$, $\Delta\Phi(\theta,t)$, and $\hat{\Gamma}(\hat{k},t)$, the Bragg matrix B can be constructed analogously to Section 3.2.3.

3 Computational Methodology

In this section, we detail the implementation of the model introduced in Chapter 2, along with the relevant computational considerations. The implementation builds upon the software framework written with `C++` developed in [2], which was originally designed for the single-crystal case. This framework includes a dedicated library, *MultiBragg*, providing a numerical solver for the transport equation. In the present study, this software has ben extended to accomodate the stack-crystal configuration, enabling the simulation of multiple coupled crystals within a unified computational framework.

3.1 Numerical Tools

To solve the system of equations in the standard form $L \cdot x = y$, a sparse LU solver is employed. The implementation utilizes components from the numerical library *Trilinos* [19, 20], in particular: the sparse compressed row matrix class from the *Epetra* package, the ILU(0) preconditioner from the *Ifpack* package [21], and the generalized minimal residual block solver from the *Belos* package [22].

3.2 Structure of the Model

In this section, we outline the general structure of the code and introduce the key variable names that will be used throughout the formulation of the problem. The implementation is primarily based on distributed sparse matrices and distributed dense vectors, realized through classes `Epetra_CrsMatrix` and `Epetra_Vector` from the *Epetra* package of the [Trilinos] library.

The unknown solution vector as well as the right-hand side of the governing equation are represented as distributed dense vectors, whereas the operator matrix L is defined as a distributed sparse matrix. This distinction is essential, as it reflects the requirements of the solver employed in this work. Nevertheless, the assembly of both the matrix L and the right-hand side vector is performed using relatively straightforward computations based on the standard `vector` class, prior to their transfer into the distributed *Epetra* structures.

In the following, we discuss in greater detail the relevant aspects of this setup, including the dimensionality of the matrices, the indexing conventions, and the separation of contributions corresponding to the forward and backward directions. It should be emphasized that the computational structure presented here corresponds to the core design of the *MultiBragg* framework [2]. The extensions developed in the course of this work are fully compatible with this design and rely on the same fundamental principles.

3.2.1 Key Components of the Model

To initialize the simulation, a set of core parameters must be specified for the model. These parameters are primarily material-dependant and include the opacity τ, the relative reflectivity ρ, the Bragg angle θ_B, and the standard deviation η of the von Mises-Fisher distribution. In addition, it is necessary to define a discretized grid on the unit sphere $\hat{k}$, which serves as the basis for the histogram bins introduced in Equation 2.6.

For this purpose, two grid parameters are introduced, denoted as n_i and n_j, which correspond to the polar (θ) and azimuthal (ϕ) subdivisions of the unit sphere, respectively. The grid is implemented as a one-dimensional array of size $M = n_i \cdot n_j$, where each entry represents a unique direction on the discretized sphere. To account for both forward and backward scattering channels, this grid is duplicated, resulting in a total size of $2M$. In this extended grid, the first M elements correspond to the forward channel ($\hat{k}_z > 0$), while the remaining M elements represent the backward channel ($\hat{k}_z < 0$). The discretization is constructed in such a way that no element is located at $\hat{k}_z = 0$. Additionally, although the azimuthal angle ϕ is defined over the full range $[-\pi, \pi]$, the polar angle θ is typically restricted to a specific interval. As a result, the grid represents a partial solid angle rather than covering the entire unit sphere.

Additionally, while the grid is defined for azimuthal angle ϕ from $-\pi$ to π, the definition of polar angle is in most cases limited to a certain interval, meaning grid returns a solid angle instead of the entire unit sphere.

With the angular grid for the scattering directions established, we can now construct the Bragg matrix B and the attenuation vector A. To this end, a crystal class introduced, which combines the material parameters with the discretized grid in order to compute both B and A. The detailed computational procedures for these quantities will be provided in Section 3.2.3; here, we restrict ourselves to the description of their structural properties.

The Bragg matrix B is represented as a vector of objects of type `BColumn`. Each `BColumn` contains two arrays: one specifying the indices of the bins from which scattering originates, and the other containing the corresponding scattering probabilites.

Once these columns are computed for all bins in the grid, the full matrix B is obtained, having dimensions $M \times M$.

For the attenuation vector A, the grid must be extended to properly account for losses within the system. This is achieved by appending three additional elements to the grid. The first element corresponds to absorption losses, parametrized by $d\mu_a$ as defined in Equation 2.61, while the remaining two represent approximation and cutoff losses introduced during the numerical computations. Following this extension, the attenuation vector A attains the size $M + 3$. Consistently, the Bragg matrix B also expends to dimensions $(M + 3) \times (M + 3)$ to reflect the augmented grid structure.

The incoming beam is likewise represented on the discretized grid. It is modeled as a perfectly collimated beam, localized to a single direction specified by the incident angles θ_{in} and ϕ_{in}.

To obtain the complete solution of the system, it is necessary to construct the full computational mesh, including the collocation points along the propogation direction. Denoting the number of collocation points by n_z, the mesh is generated by extending the previously defined angular grid. The resulting mesh thus contains a total of $(2M + 3) \cdot n_z$ degrees of freedom.

For the numerical implementation, a class named `MatrixTask` is employed. This class takes as the input the crystal parameters, the mesh, and the incident beam definition. From these, it constructs both the operator matrix L and the right-hand side vector of the governing equation. The resulting linear system is then solved using the solver introduced earlier.

The *MultiBragg* library also provides an iterative refinement scheme in which n_z is progressively increased until the change between successive solutions falls below a specified tolerance. In the present work, however, we prefered to use the main function with fixed n_z, as this approach allows for more systematic control when comparing different numerical cases. An overview of the components described in this section is given in Table 3.1.

3.2.2 Computing Matrix L

The computation of the matrix L follows the definition introduced in Equation 2.25. The differentiation matrix D is constructed according to the procedure outlined in Section 2.1.4, using the definitions provided in Equations 2.21, 2.22, and 2.23, respectively. The calculation of the Bragg matrix B and the attenuation vector A is described in detail in Section 3.2.3; for the present discussion, both structures are treated as having arbitrary entries within physically plausible ranges. In numerical implementation, the Kronecker deltas δ_{ij} appearing in Equation 2.25 act as operators that extract the diagonal elements from their respective matrices, thereby ensuting

Table 3.1: Overview of the key components of the model.

Component	Notation	Input Parameters
Grid size in θ	n_i	-
Grid size in ϕ	n_j	-
Grid	`G`	n_i,n_j
Number of collocation points	n_z	-
Mesh	`M`	`G`,n_z
Crystal	`crystal`	τ,ρ,θ_B,η,`G`
Incoming Beam	I_{in}	`G`, θ_{in}, ϕ_{in}

consistency of matrix dimensions throughout the computations. Finally, since the resulting matrix L is sparse due to the Kronecker deltas, it is implemented using the `Epetra_CrsMatrix` class. An illustration of the matrix L, highlighting its structure under the chosen angular and collocation discretization scheme, is presented in Figure 3.1.

For the stack case, it is necessry to compute a total matrix L_{tot} that represents the entire system. To this end, the matrix L is first calculated for each crystal. In this configuration, the only differences between crystal arise from the Bragg matrix B and the attenuation vector A; hence, the computation for each crystal proceeds analogously to the single-crystal case. Once the individual matrices $L^{\mathcal{N}}$ have been obtained, they are assembled into a block-diagonal matrix, with each $L^{\mathcal{N}}$ placed along the diagonal in the appropriate order. Finally, the coupling vectors are appended to the system matrix, yielding the complete equation system with the boundary conditions specified in Equation 2.69.

3.2.3 Computing Bragg Matrix and Attenuation Vector

By combining Equations 2.8 and 2.52, the Bragg matrix element B_{ms} is obtained as

$$B_{ms} = \bar{\mu} \cos\theta_B \int_0^{2\pi} dt W(\hat{\Gamma}(\hat{k}, t)) \quad \text{for} \quad \hat{\kappa}(\hat{k}_s, t) \in \Delta\Omega_m. \tag{3.1}$$

For a fixed $\hat{k}_s$ and t, the deflection function $\hat{\kappa}(\hat{k}_s, t)$ describes a one-dimensional-manifold on the two-dimensional unit sphere [2]. As a result the Bragg matrix B acquires a sparse structure. Moreover, the restriction imposed by the condition at the end of the formulation ensures that the integral only accounts for deflections that fall within the corresponding grid element. While this does not pose a problem for normal oriented crystals, it leads to certain deflections falling outside the predefined grid space

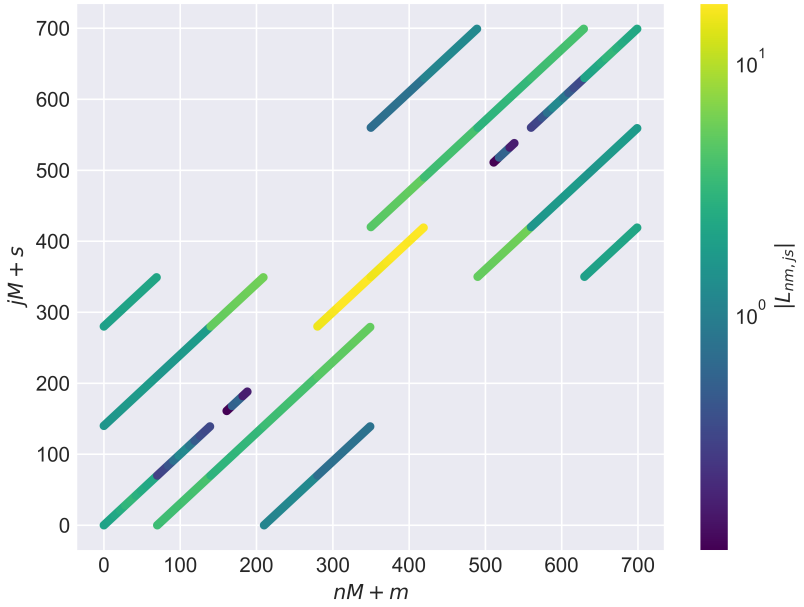

Figure 3.1: Visualization of the matrix L. The discretization employs five collocation points, ten bins for $\theta \in [60°, 80°]$, and thirty six bins for $\phi \in [-180°, 180°]$. The material parameters are set to $\theta_B = 70°$, $\rho = \tau = 1$ and $\eta = 2.5°$. As certain matrix entries assume negative values, the absolute values $|L_{nm,js}|$ are depicted..

in the case of tilted crystals, since the tilting angle χ causes an additional angular shift in the grid. These numerical losses, however, are accounted for through the second loss channel mentioned in Section 3.2.1.

To evaluate the integral in Equation 3.1, the integration domain is subdivided into intervals using a recursive bisection method. The points $t_0 = 0 < t_1 < ... < t_{l_1} < t_l = 2\pi$ are determined such that, for each $t \in [t_f, t_{f+1}]$, all values of the deflection function $\hat{\kappa}(\hat{k}_s, t)$ fall within a single bin ρ_{sf}. This subdivision is continued until the interval length becomes smaller than $\frac{\eta}{5}$. With this discretization, Equation 3.1 reduces to

$$B_{ms} = \bar{\mu} \cos\theta_B \sum_{f=0}^{l-1} \int_{t_f}^{t_{f+1}} dt W(\hat{\Gamma}(\hat{k}, t)) \quad \text{for} \quad \rho_{sf} = m. \tag{3.2}$$

Since the integration intervals are now very small, each integral is efficiently approximated using Gauss-Legendre three-point quadrature [2]. The deflection function $\hat{\kappa}(\hat{k}_s, t)$ is evaluated at the midpoint $t = \frac{t_{f+1} - f_l}{2}$, allowing the corresponding bin $\rho_s f$ to be identified and incremented appropriately to determine the correct deflection mapping.

As an example, Figure 3.2 depicts the Bragg matrix B, illustrating the variation of its columns with respect to different scattering angles. This figure serves to clarify the structure of the matrix and its role in representing the angular-dependent scattering behavior in the model.

To further increase the sparsity of B, the matrix entries below a prescribed tolerance are set to zero. Specifically, B_{rs} is discarded whenever

$$B_{rs} < \epsilon_K \max(B_{rs}/M), \tag{3.3}$$

where tolerance is defined as $\epsilon_K = 10^{-5}$ [2]. The numerical losses resulting from this truncation are consistently recorded in the third loss channel.

In the case of vanishing absorption, i.e. $\mu_a = 0$, the total current along the $\hat{e}_z$-direction is conserved,such that

$$\partial_z \sum_{m=1}^{M} \hat{k}_{m,z} I_m(z) = 0. \tag{3.4}$$

To preserve the condition even in the presence of non-diffractive losses, an additional grid element is introduced, denoted as the *loss channel* $I_a(z)$. Numerical experiments indicate that the preferred propogation direction of this channel is backwards, i.e. $\hat{k}_a = -\hat{e}_z$, which leads to the boundary condition $I_a(d) = 0$ [2]. The inclusion if this channel modifies the Bragg matrix B by introducing the entries

$$\begin{aligned} B_{as} &= \mu_a \quad \text{for} \quad s \neq a, \\ B_{ma} &= 0 \quad \text{for all } m. \end{aligned} \tag{3.5}$$

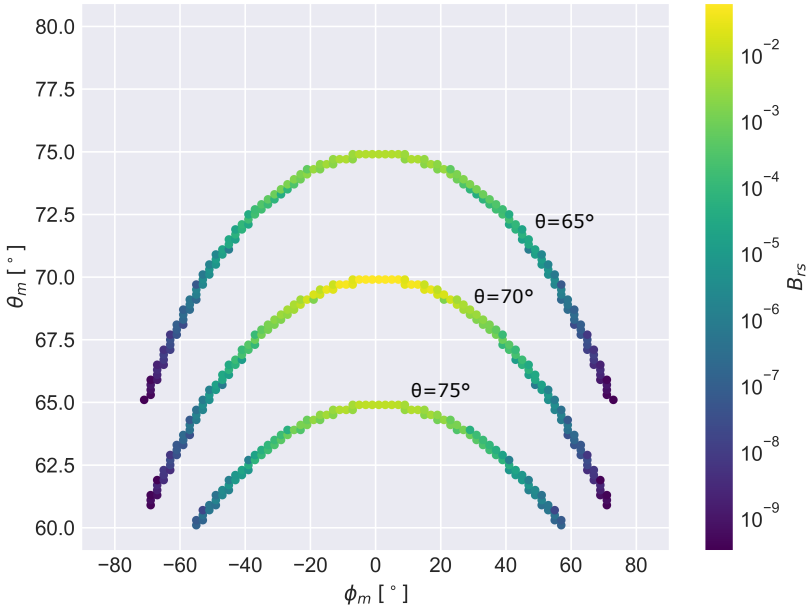

Figure 3.2: Bragg matrix B visualized for three scattering angles, $\theta_s = 65°, 70°, 75°$, with $\phi_s = 0°$. The three bands indicate the matrix columns corresponding to the respective θ_s values. The Bragg angle is $\theta_B = 70°$, standart deviation is $\eta = 2.5°$, and $\rho = \tau = 1$ is used for simplicity. The angular grid comprises 180 bins for ϕ over $[-180°, 180°]$ and 100 bins for θ over $[60°, 80°]$.

such that the attenuation vector is no longer explicitly dependent on μ_a, but instead becomes

$$A_m = \sum_{s=1}^{M} B_{sm}. \tag{3.6}$$

In addition to the absorption channel, two further loss channels, $I_b(z)$ and $I_c(z)$, are introduced to account for numerical losses incurred during the discretization and approximation procedures described in Section 3.2.1. The second channel, $I_b(z)$, represents deflections that fall outside the angular grid. This occurs due to the finite resolution in the polar angle θ, which renders the integral in Equation 2.7 inexact, such that for certain s there exists a probability B_{bs} of diffraction into direction $\hat{k}'$ not represented in the grid [2]. The third channel, $I_c(z)$, collects losses arising from the sparsification of the Bragg matrix, where entries B_{ms} below a given tolerance are set to zero. In this case, the deleted entries are summed, and the corresponding contribution is assigned to B_{cs} for the given s.

The computation of the Bragg matrix B and the attenuation vector A for tilted crystals is carried out within the same general framework as outlined above, with the only modification being the application of the reformulations introduced in Section 2.2.2, in place of the single-crystal case. However, the current implementation leads to substantial increase in the loss channel $I_b(z)$. Specifically, crystal tilting results in a significant portion of the flux being deflected outside of the discretized grid. This effect also obscures the distinction between whether the losses originate from transmission or reflection processes. At present, we restrict ourselves to noting this limitation and proceed with the analysis while carefully accounting for its impact on the results. A more refined treatment or corrective strategy will be left as a subject for future work.

3.3 Hyperparameters and Tolerances

While the present work primarily focuses on extending the existing single-crystal model [2] to the case of stacked crystals, its accuracy is assessed qualitatively by comparison with the single-crystal results. For completeness, potential sources of error are briefly discussed here, together with the relevant hyperparameters and numerical tolerances, without providing further derivations. More detailed explanations can be found in [2].

The numeric solution is governed by hyperparameters and tolerances:

1. **Angular discretization:** Bounds of θ and ϕ, and the number of bins used for the directional grid.

2. **Collocation points:** In the original single-crystal model, the initial number of collocation points and the increment for the iterative scheme were treated as hyperparameters. In the present work, however, we employ a fixed number of collocation points, chosen consistently with the single-crystal model to allow direct comparison. Thus, in the stack case, the number of collocation points can be regarded as a hyperparameter. The chosen value corresponds to the optimal number determined in its corresponding single-crystal model.

3. **Auxiliary parameters for the computation of B:** Bisection accuracy $\delta t = 10^{-15}$, maximum step size $\frac{\Delta t}{\eta} = 0.2$, and the kernel cutoff $\epsilon_K = 10^{-5}$.

4. **Collocation tolerance:** In the single-crystal model, the iterative scheme includes a collocation tolerance $\epsilon_C = 10^{-5}$ to determine convergence. Although this tolerance does not directly apply to the stack model, it is retained here for completeness, as the number of collocation points in the stack case was chosen on the basis of the single-crystal model with this tolerance.

5. **Solver tolerance:** $\epsilon_S = 10^{-7}$ for the sparse equation solver provided by *Trilinos*.

6. **Numerical integrity checks:** A noise level $\epsilon_N = 10^{-5}$, stricter limit $\epsilon_F = 10^{-4}$, and cutoff tolerances $\epsilon_B = \epsilon_C = 10^{-4}$ are applied to ensure the numerical consistency of the obtained solutions with respect to the loss channels.

3.4 Chosen Parameters for the Model

The material parameters, along with the selected hyperparameters employed in this model, are summarized in Table 3.2. The number of collocation points n_z, was determined by performing single-crystal simulations using the iterative scheme to identify the optimal discretization. Based on the analysis, $n_z = 12$ was selected. For the stack case, in order to explore different configurations, we tested $n_z = 4$ and $n_z = 12$ per crystal, corresponding to a total of $n_{z,\text{tot}} = 12$ and $n_{z,\text{tot}} = 36$, respectively. The number of bins in the angular grid is chosen according to the specific type of calculation being performed and is specified individually for each result, whereas the range of the polar domain is fixed and given in Table 3.2. All remaining parameters were kept the same unless otherwise specified.

Table 3.2: Summary of the material parameters and their corresponding values employed in the model.

Parameter	Value
Grid `G`	$[\theta_B - 4\eta, \theta_B + 4\eta]$
Number of collocation points n_z	12
Opacity τ	1
Relative reflectivity ρ	1
Standard deviation η	2.5°
Bragg angle θ_B	70°
Incoming Beam I_{in}	$\theta_{\text{in}} = \theta_B$, $\phi_{\text{in}} = 0°$
Tilting angle χ	2.5°
Number of crystals in stack case $\mathcal{N}_{\text{tot}}$	3

4 Results and Discussion

In this section, we present and analyze the results obtained from the extended model for the stack case, in comparison with the previously established single-crystal model. We begin by verifying the effect of crystal tilting through an initial analytical analysis. Subsequently, we examine the numerical results produced by the developed model, highlighting its performance as well as the sources and implications of numerical errors wherever possible. Following this, we present the test results for the current stack crystal implementation. As noted previously in Section 2.2, the present stack model lacks a proper reflection coupling mechanism, which leads to significant deviations from the behavior predicted by the equivalent single-crystal model. Based on these observations, we provide suggestions for improvements and potential refinements to address the limitations identified in the current results.

4.1 Crystal Tilting

4.1.1 Polar Deflection and Azimuthal Shift Functions

Before proceeding with the full simulations, it was essential to validate the newly developed transformation of the polar deflection function $\Theta(\theta, t)$ and the azimuthal shift function $\Delta\Phi(\theta, t)$, as defined in Equation 2.78, by comparing them with their counterparts in the normal-oriented case given in Equation 2.50. This validation step ensures that the tilting transformation is consistent with the Bragg matrix formalism introduced in Section 2.1.5, where the scattering geometry was described using rotation matrices. Since the Bragg matrix inherently describes how the incident wavevector is mapped onto the scattered one under the Bragg condition, any modification of the crystal orientation must consistently manifest in the resulting scattering functions.

We begin by examining the polar deflection function $\Theta(\theta, t)$. Figure 4.1 presents a comparison between $\Theta_{\text{normal}}(\theta, t)$ and $\Theta_{\text{tilted,2.5}^\circ}(\theta, t)$ for five different incident angles θ_{in} with $\phi_{\text{in}} = 0^\circ$. In the normal orientation, one observes that the difference between scattering angle $\Theta(\theta, t)$ and the Bragg angle θ_B increases as the incident angle θ_{in} moves further away from the Bragg angle θ_B. This behavior is consistent with the Bragg condition, where deviations from the exact Bragg angle shift the scattering vector and lead to a larger deflection angle. The Bragg matrix calculations performed earlier

already indicated this sensitivity of the scattering geometry to deviations in θ_{in}, and the present comparison confirms the expected trend on a functional level.

Once the crystal is tilted by $\chi = 2.5^\circ$, a systematic shift in the scattering directions appears. Physically, this tilt alters the reflection condition in the crystal's local reference frame relative to the laboratory frame. The Bragg matrix formalism predicts that such a rotation introduces additional misalignment term, effectively reducing the polar scattering angle in the laboratory frame. Indeed, the comparison shows that, across all incident angles, the scattered rays are deflected by approximately 5° less compared to the normal oriented case. Additionally, difference between each incoming angles θ_{in} is around 2.5° in the normal oriented case, while in the tilted case this difference becomes less than 2.5°. This reduction is not uniform across the azimuthal domain, which emphasizes that tilting does more than just inroduce a constant offset, it reshaps the angular dependence in $\Theta(\theta, t)$.

The relative change between the normal and tilted cases is quantified in Figure 4.2. The curves demonstrate that while the difference is minimal in the outer azimuthal regions $t \in [-180^\circ, -90] \cup [90^\circ, 180^\circ]$, the effect is most pronounced in the central region $t \in [-60^\circ, 60^\circ]$. From the standpoint of the Bragg matrix formulation, this is precisely the regime where the azimuthal contributions are most strongly coupled to the polar deflection. Importantly, this central domain coincides with the region weighted by the Mises-Fisher distribution $W(\hat{\Gamma}(\hat{k}, t))$, which enters directly into the integral formulation of the scattering probability in Equation 3.2. Hence, the observed modification due to tilting is not a marginal effect but one that significantly alters the effective contribution of the scattering process to physically measurable quantities.

Another point worth noting is the interplay between the tilt and the dependence on the incident angle θ_{in}. For incident angles close to the Bragg angle, the difference between the normal and tilted cases is significant, while for larger deviations from θ_B, the reduction in $\Theta(\theta, t)$ becomes negligible. This observation reinforces the role of tilting as a perturbation to the Bragg condition: while the Bragg angle itself remains the reference point, the effective angular acceptance of the reflection is reshaped. Such reshaping is consistent with the predictions from the Bragg matrix formulation, where the introduction of an additional rotational degree of freedom shifts the directions of the scattering transformation.

In summary, the comparison between the normal and tilted orientations confirms consistency of the newly developed transformation with the Bragg matrix framework. The results show that tilting does not simply shift the scattering angle uniformly but inroduces a structured modification that primarily affects the physically relevant azimuthal region. This finding has two important implications for the simulations to follow: (i) the angular redistribution caused by tilting must be explicitly accounted for in order to obtain accurate predictions of the scattering intensities, and (ii) regions of

negligible difference, such as the outer azimuthal domains, can be disregarded.

A brief investigation was conducted to assess the effect of crystal tilting on the azimuthal shift function $\Delta\Phi(\theta, t)$. Similar to the analysis of the polar deflection function $\Theta(\theta, t)$, we compared the shift functions for a normal oriented crystal and a tilted crystal with $\chi = 2.5°$. The results, shown in Figure 4.3, indicate that crystal tilting has no significant effect on $\Delta\Phi(\theta, t)$, as anticipated. This outcome is consistent with the fact that the tilt angle $\chi = 2.5°$ lies within the small -angle approximation regime, where $\cos\chi \approx 1$ and $\sin\chi$ can be neglected. The only potential source of non-negligible change arises from the $\cos(\theta - \chi)$ term in Equation 2.78; however, this contirbution remains minor. Figure 4.4 illustrates the relative difference between the normal and tilted cases. The maximum deviation occurs at $\pm 180°$, while the difference is nearly zero within the interval $t \in [-60°, 60°]$, which corresponds to the region where the dominant scattering events occur. In summary, these results demonstrate that the azimuthal shift is effectively invariant under crystal tilting, thereby confirming that the symmetry of the angle ϕ is practically preserved.

4.1.2 Bragg Matrix under Crystal Tilting

Having verified the consistency of the tilted crystal formulation, we now turn to the construction of the Bragg matrix B under crystal tilting. For this purpose, two otherwise identical crystals are considered, each tilted by opposite angles $\chi_{\pm} = \pm 2.5°$, with the material parameters specified in Table 3.2. Their results are then directly compared to the corresponding case of a normal-oriented crystal with identical parameters. This comparison allows us to assess how the tilt is incorporated into the Bragg matrix formalism and to confirm that the transformation remains consistent with the underlying symmetry relations.

Figures 4.5, 4.6 and 4.7 present the Bragg matrices for the normal oriented crystal and for the crystals tilted by $\chi_+ = +2.5°$ nd $\chi_- = -2.5°$, respectively. In all three cases, the scattering directions are correctly represented within the angular grid, and the weighting distribution $W(\hat{\Gamma}(\hat{k}, t))$ is applied consistently relative to the normal oriented reference case shown in Figure 4.5. A particularly instructive validation of this consistency is given by the proper reproduction of Bragg reflections under tilting. For the positively tilted crystal, an incoming angle of $\theta_{\text{in}} = 72.5°$ is scattered into the Bragg angle $\theta_B = 70°$. Conservely, for the negatively tilted crystal, the Bragg condition is fulfilled at $\theta_{\text{in}} = 67.5°$. This behavior follows directly from the angular transformation into the local crystal reference frame: in the positive tilt case, $\theta_{\text{in}} = 72.5°$ is shifted to an effective $\theta'_{\text{in}} = 70°$, thereby satisfying the Bragg condition, while the opposite occurs for the negative tilt.

An important observation, however, emerges during the construction of the Bragg

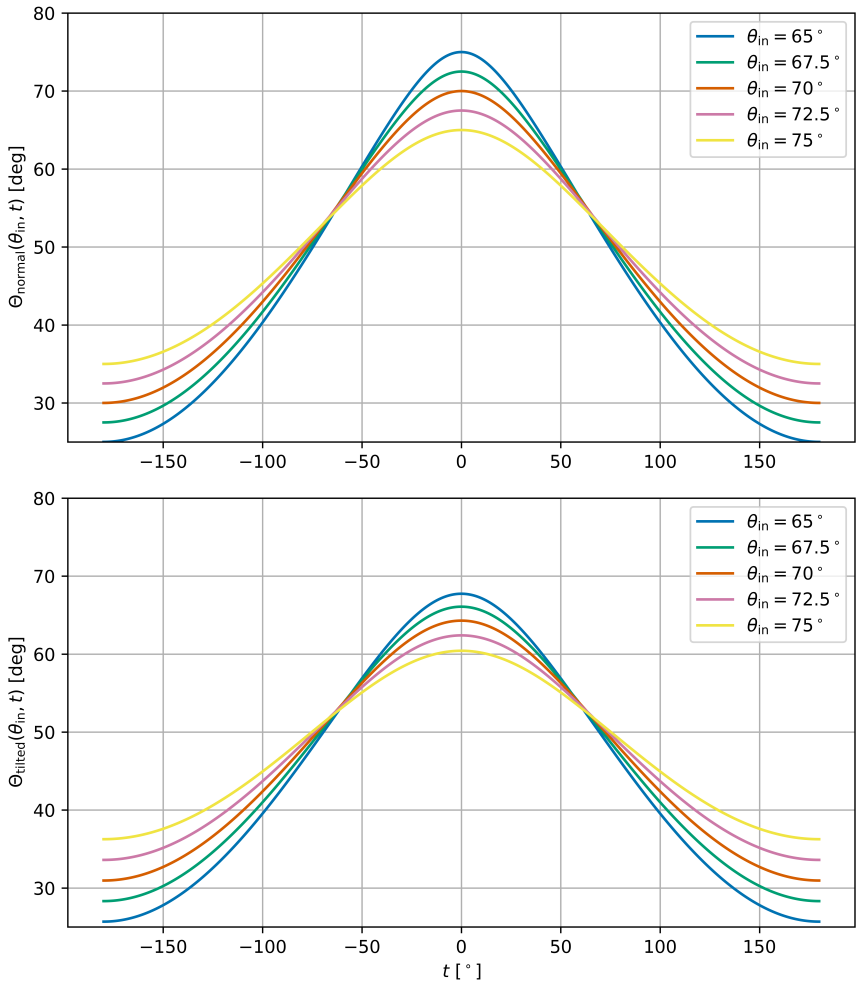

Figure 4.1: Comparison of the polar deflection function $\Theta(\theta, t)$ in the normal orientation (top) and with a crystal tilt of $\chi = 2.5^\circ$ (bottom) for five different incident angles θ_{in} with $\phi_{\text{in}} = 0^\circ$. In the normal case, the angular difference $\theta_{\text{out}} - \theta_B$ grows as θ_{out} deviates from the Bragg angle θ_B. Tilting systematically reduces the scattering angle by 5° and reshapes the angular dependence, with the strongest deviations occurring in the azimuthal domain around $t = 0^\circ$.

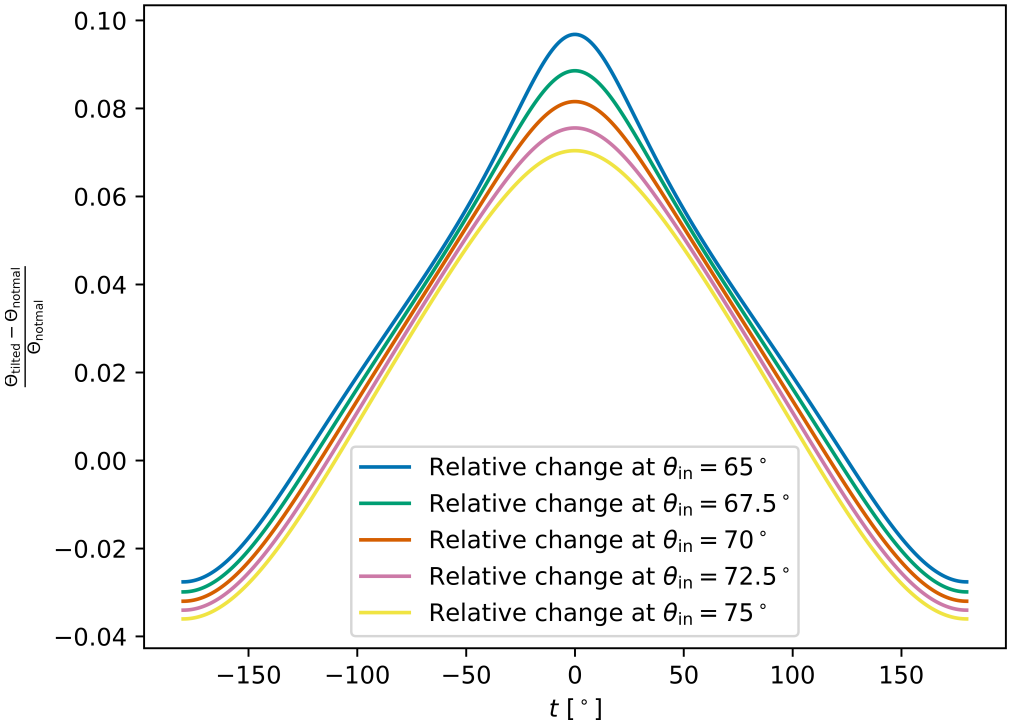

Figure 4.2: Relative change of the polar deflection function $\Theta(\theta, t)$ between the normal-oriented case $\Theta_{\text{normal}}(\theta, t)$ and the tilted case $\Theta_{\text{tilted},2.5^\circ}(\theta, t)$ for five different incident angles θ_{in} with $\phi_{\text{in}} = 0^\circ$. The curves demonstrate that the effect of tilting is negligible in the outer azimuthal regions, while the central range $t \in [-60^\circ, 60^\circ]$ exhibits a pronounced modification of the scattering angles.

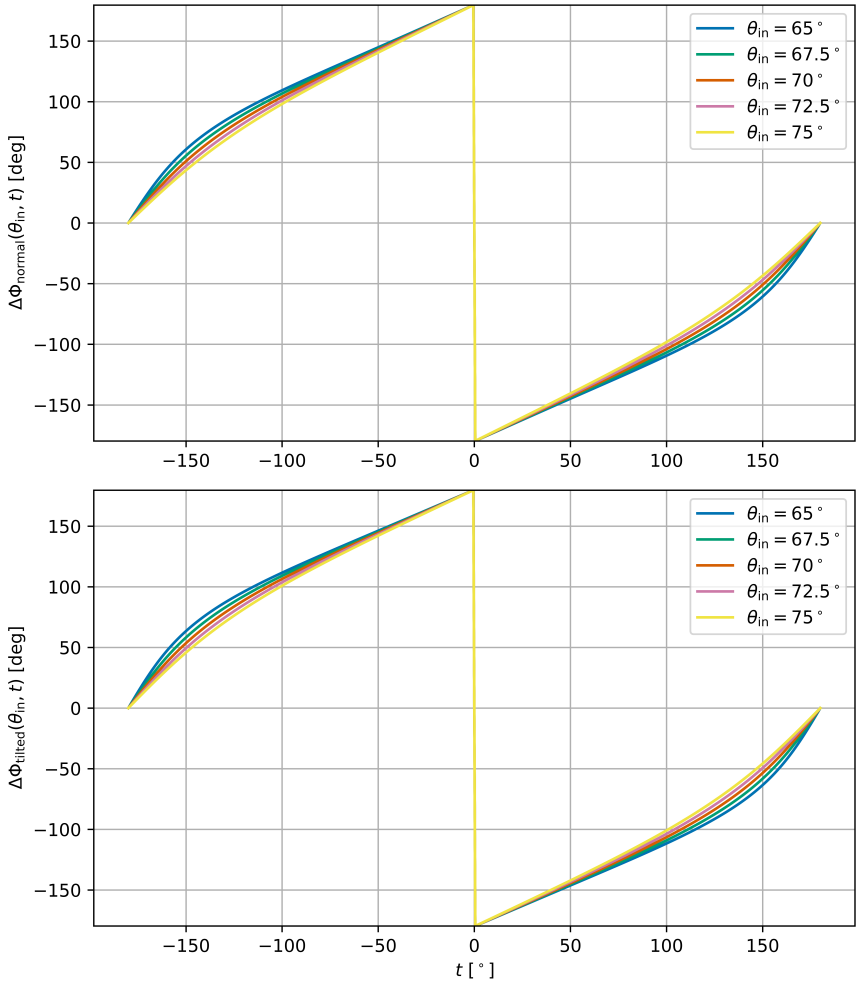

Figure 4.3: Comparison of the azimuthal shift function $\Delta\Phi(\theta, t)$ in the normal orientation (top) and with a crystal tilt of $\chi = 2.5^\circ$ (bottom) for five different incident angles θ_{in} with $\phi_{in} = 0^\circ$. Both cases show the characteristic discontinuity at $t = 0^\circ$, which reflects the branch cut in the azimuthal transformation. While the overall functional form is preserved under tilting, negligible deviations appear across the azimuthal domain.

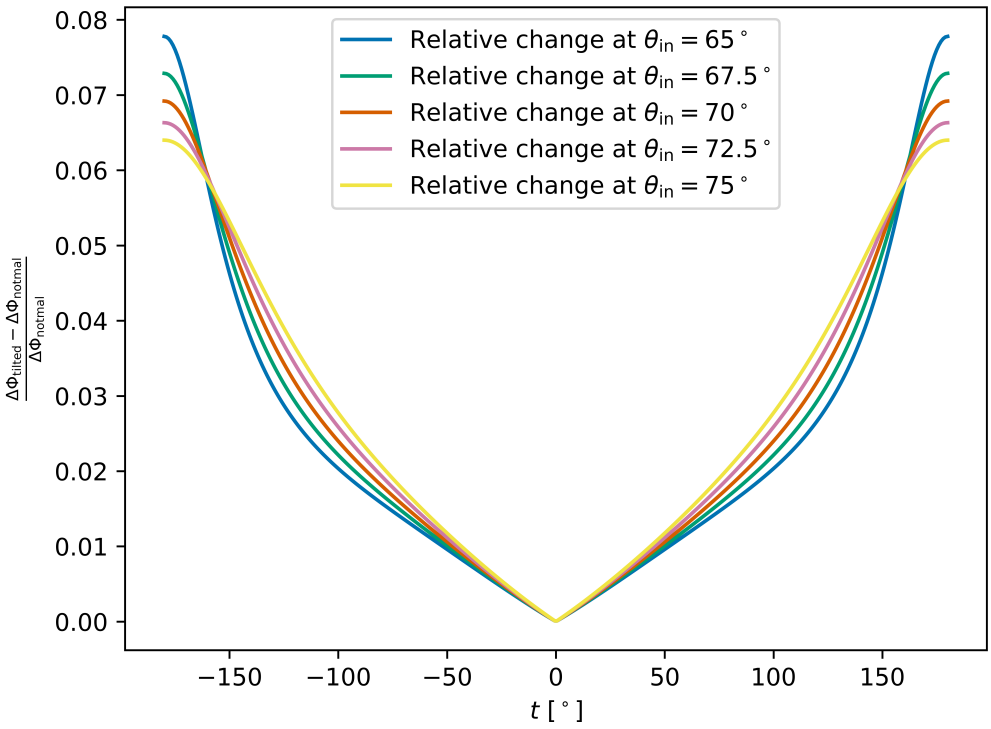

Figure 4.4: Relative change of the azimuthal shift function between the tilted case and the normal orientation, $(\Delta\Phi_{\text{tilted}}.\Delta\Phi_{\text{normal}})/\Delta\Phi_{\text{normal}}$, for five different incident angles θ_{in} with $\phi_{\text{in}} = 0°$. The alrgest deviations occur in outer azimuthal regions $t \approx \pm 180°$, while the central domain around $t = 0°$ is largely unaffected by tilting. The magnitude of the relative change depends weakly on θ_{in}.

matrices for the tilted crystals. Despite the correct reproduction of the scattering geometry, matrix elements associated with the normal oriented case appear in the tilted matrices. This results in additional, spurious scattering probabilites in angular regions where no scattering events should occur. The presence of such duplicate contributions violates probability conservation, which is a critical condition for obtaining physically consistent results. These artificial scattering channels are visible in Figures 4.6 and 4.7, where the tilted cases exhibit redundant reflection entries.

Given the earlier verification of the deflection and shift functions in Section 4.1.1, where no inconsistencies were found, the origin of this problem is most likely related to the computational implementation rather than the theoretical framework. Specifically, the issue appears to arise in the numerical construction of the Bragg matrix, particularly in the implementation of the reflection and bisection procedures described Section 3.2.3. Possible causes include erroneous bin assignments of scattering directions in the reflect function or inaccuracies in the evaulation of the angular integrals for tilted crystals within the bisection method.

The implications of this violation of conservation are non-negligible, as they directly affect the physical plausibility of the resulting scattering intensities. A detailed discussion of the consequences of these inconsistencies, as well as their effect on the total reflectivity of tilted crystals, is provided in Section 4.1.3.

4.1.3 Total Reflectivity and Violation of Probability Conservation

Having constructed the Bragg matrices for the tilted crystal cases, we now turn to a simple but illustrative example: the calculation of the total reflectivity of tilted crystals compared to the normal-oriented reference case, with particular attention to the consequences of the violated probability conservation observed earlier.

For this analysis, the incident angle θ_{in} is swept over the range $65^\circ \leq \theta_{\text{in}} \leq 75^\circ$ with an increment of 0.25°. The results for the normal orientation, as well as for tilts of $\chi_+ = +2.5^\circ$ and $\chi_- = -2.5^\circ$, are presented in Figures 4.8, 4.9 and 4.10, respectively. The normal oriented case (Figure 4.8) serves as a reference: as expected, the total reflectivity reaches its maximum at the Bragg angle θ_B, while the total transmission simultaneously reaches a minimum. The attenuation is negligible in this configuration, confirming that probabilty is conserved within the Bragg matrix and that all flux is properly partitioned into reflection and transmission channels.

The situation changes markedly for the tilted cases. As discussed in Section 4.1.1, the construction of the tilted Bragg matrices introduces duplicate entries, which generate unphysical scattering channels. These additional contributions break probability conservation, thereby leaading to artificial losses in the system. The effect is visible in Figures 4.9 and 4.10. Under ideal conditions, one would expect the reflectivity curve of

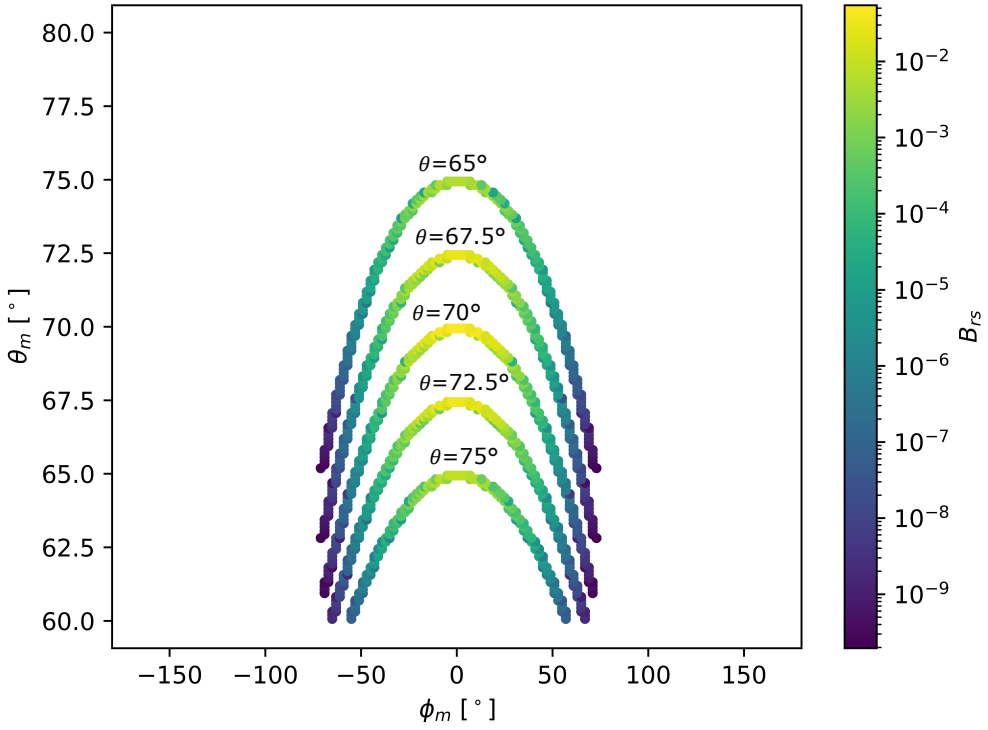

Figure 4.5: Bragg matrix B of the normal oriented crystal, visualized for five scattering angles, $\theta_s = 65°, 67.5°, 70°, 72.5°, 75°$, with $\phi_s = 0°$. The bands indicate the matrix columns corresponding to the respective θ_s values. The used material parameters are given in Table 3.2. The angular grid comprises 180 bins for ϕ over $[-180°, 180°]$ and 160 bins for θ over $[60°, 80°]$.

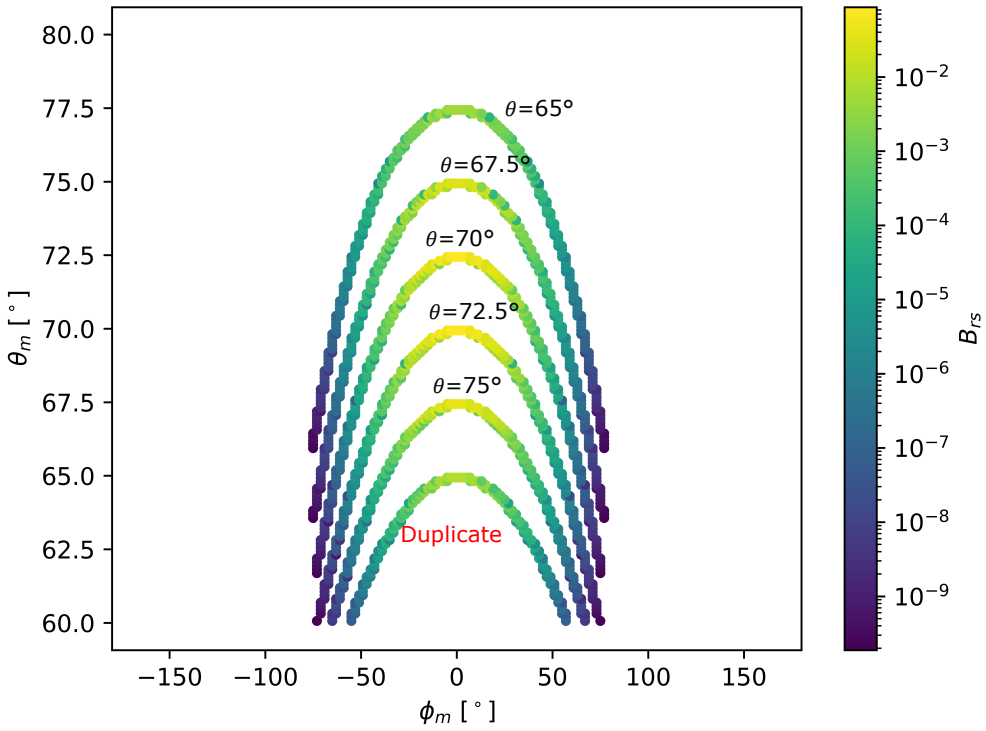

Figure 4.6: Bragg matrix B of the crystal with tilting $\chi_+ = +2.5°$, visualized for five scattering angles, $\theta_s = 65°, 67.5°, 70°, 72.5°, 75°$, with $\phi_s = 0°$. The bands indicate the matrix columns corresponding to the respective θ_s values. The used material parameters are given in Table 3.2. The angular grid comprises 180 bins for ϕ over $[-180°, 180°]$ and 160 bins for θ over $[60°, 80°]$. The duplicate entries are shown with the red label.

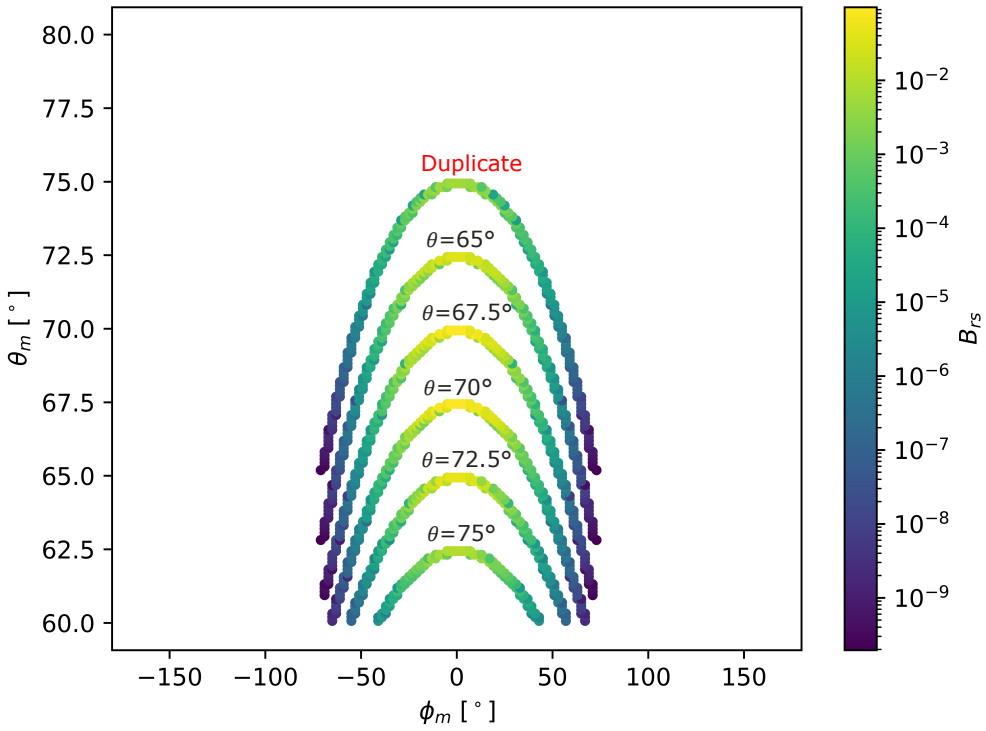

Figure 4.7: Bragg matrix B of the crystal with tilting $\chi_- = -2.5°$, visualized for five scattering angles, $\theta_s = 65°, 67.5°, 70°, 72.5°, 75°$, with $\phi_s = 0°$. The bands indicate the matrix columns corresponding to the respective θ_s values. The used material parameters are given in Table 3.2. The angular grid comprises 180 bins for ϕ over $[-180°, 180°]$ and 160 bins for θ over $[60°, 80°]$. The duplicate entries are shown with the red label.

a tilted crystal to resemble the normal oriented case, but shifted such that the maximum reflectivity occurs around $\theta_{\text{in}} \approx \theta_B + \chi$. Instead, the computed results exhibit strong attenuation and distorted curve shapes, which deviate significantly from the expected shifted profile.

The attenuation visible in both tilted cases indicates that a large fraction of the flux that should contribute to the reflection maximum is instead registered as losses. In addition, part of the transmitted flux is also misclassified as attenuation. While the computational framework tracks these losses through the second loss channel $I_b(z)$, it does not retain information about whether the lost flux originates from reflection or transmission outside the angular grid. As a result, a detailed physical interpretation of the attenuation is not possible. Nonetheless, a residual shift of the reflectivity curves can still be discerned, albeit in the wrong direction, further underscoring the presence of numerical inconsistencies.

The underlying cause of this anomalously high attenuation lies in the duplicate entries within the Bragg matrix. As shown in the attenuation calculation of Equation 3.6, the attenuation vector is obtained directly from the Bragg matrix elements as the sum over all scattering entries. In the normal oriented case, the largest element of this vector remains on the order of 10^{-1}, consistent with physically acceptable loss levels. In contrast, for the tilted crystals the presence of duplicate entries causes certain attenuation elements to exceed unity, which is unphysical and corresponds to unrelistic losses. As a result, redundant scattering directions originating from the normal oriented case persist in the tilted matrices, leading to a missallocation of flux. This faulty construction of the attenuation vector directly violates probability conservatin for the scattering events and prevents the extraction of physically meaningful reflectivity data.

4.2 Stack Model

We now turn our attention to the stack model. Owing to the issues identified for tilted crystals, the following discussion is restricted to stacks composed of normal oriented crystals. As previously emphasized, one of the principal shortcomings of the current framework is the abscence of a suitable reflection-coupling element that would allow backward-propogating flux to be transferred consistently to the top of the first crystal. In its present form, this omission prevents the total reflectivity of the stack from being properly captured.

A secondary but closely related consequence arises from this limitation: since internal reflections within the stack are not correctly represented, their contribution to the overall transmission is also missing. This leads to a systematic underestimation of both reflection and transmission, thereby compromising the physical reliability of the model.

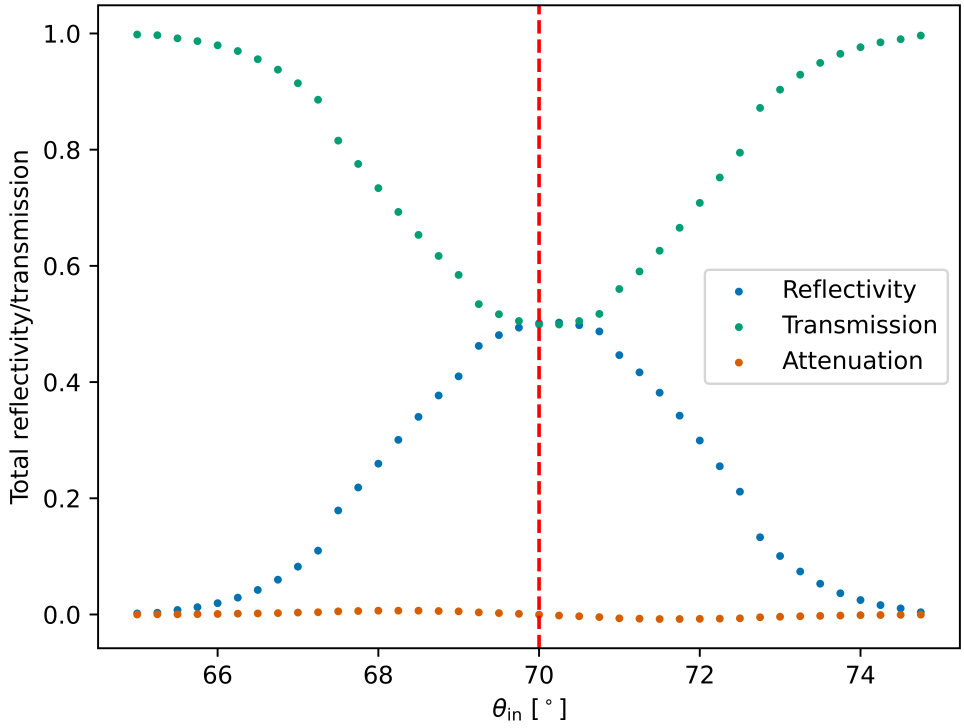

Figure 4.8: Total reflectivity, transmission, and attenuation as a function of the incoming angle θ_{in} for the normal-oriented crystal. The maximum reflectivity and minimum transmission occur at the Bragg angle θ_B, indicated by the vertical red line. Attenuation remains negligible, confirming probability conservation in this case. Number of bins chosen as $n_i = 91$ and n_j=1.

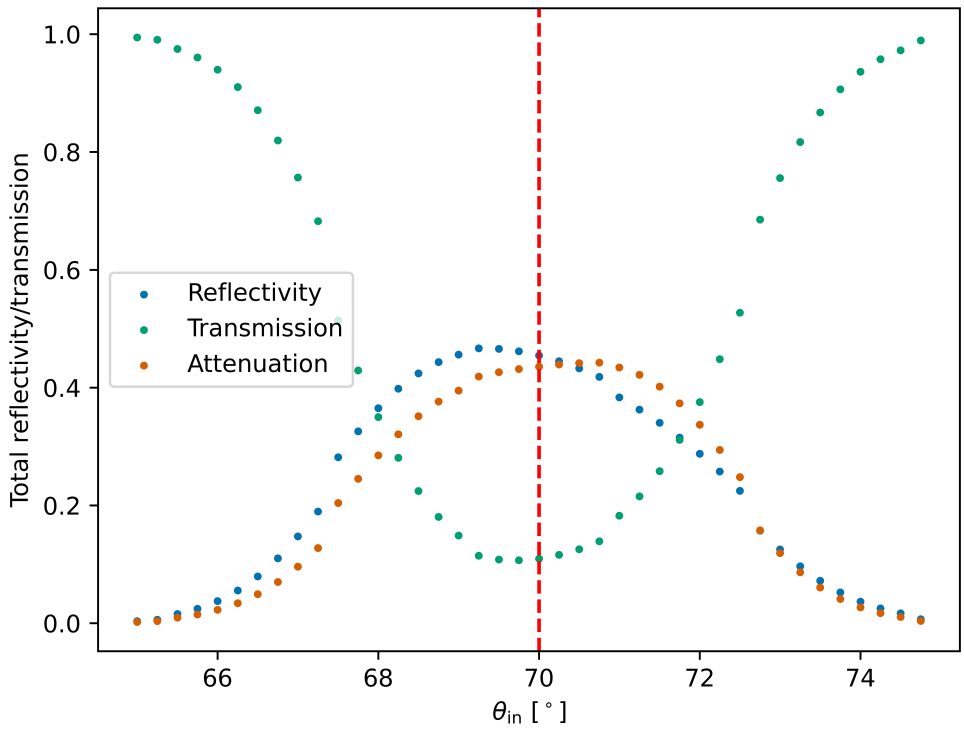

Figure 4.9: Total reflectivity, transmission, and attenuation as a function of the incoming angle θ_{in} for the crystal tilted by $\chi_+ = +2.5°$. The Bragg angle θ_B is indicated by the vertical red line. In contrast to the normal-oriented case, the reflectivity curve does not simply shift towards $\theta_{\text{in}} \approx \theta_B + \chi$, but instead exhibits strong attenuation due to the violation of probability conservation caused by duplicate entries in the Bragg matrix. Number of bins chosen as $n_i = 91$ and n_j=1.

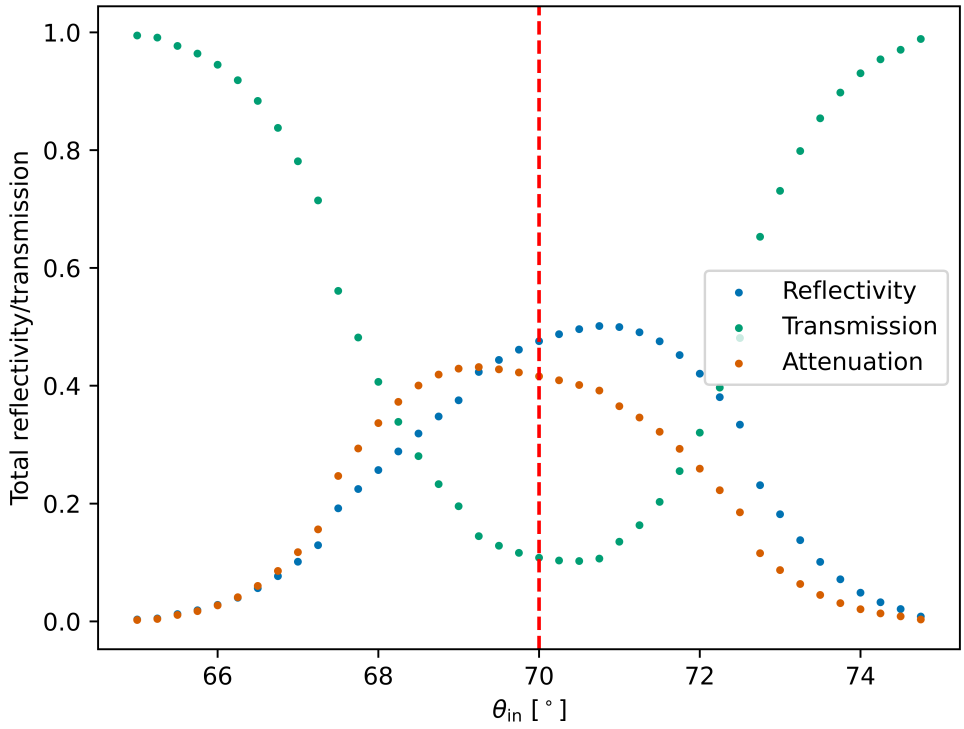

Figure 4.10: Total reflectivity, transmission, and attenuation as a function of the incoming angle θ_{in} for the crystal tilted by $\chi = -2.5°$. The Bragg angle θ_B is indicated by the vertical red line. Similar to the positively tilted case, the reflectivity curve does not simply shift to $\theta_{\text{in}} \approx \theta_B + \chi$, but instead shows pronounced attenuation arising from the violation of probability conservation due to duplicate entries in the Bragg matrix. Number of bins chosen as $n_i = 91$ and n_j=1.

The coupling vectors introduced in Section 2.2 partially address the problem by ensuring continuity of the flux between the interfaces. However, in the abscence of a reflection condition at the interfaces, the model implicitly assumes that no reflection occurs at the termination of each crystal. This assumption disrupts the natural propogation of reflected waves through the stack and effectively cancels the fluidity of reflection across the entire system. A proper implementation of reflection-coupling at each interface is therefore required to achieve a physically consistent description of stacked crystal systems.

Nevertheless, we presented the results of the stack model in comparison to its corresponding single-crystal case, as shown in Figure 4.11. In particular, a stack of three crystals of thickness d, each with an opacity of $\tau = 1$, should ideally correspond to a single crystal of thickness $3d$ and total opacity $\tau = 3$. However, when comparing the two cases, the total reflectivity of the systems do not match, while the curve shape is same for both cases. The primary reason for this discrepancy lies in the abscence of a reflection coupling mechanism, as discussed earlier.

A further comparison between the stack model and a single crystal with $\tau = 1$ shows exact agreement, which comfirms that the contributions from reflections within the additional two crystals of the stack are not accounted for the current implementation. This finding reinforces the interpretation of the abscence of the reflection processes across crystal interfaces.

We also investigated the effect of the number of collocation points n_z on the accuracy of the computation, as illustrated in the bottom-right panel of Figure 4.11. It is evident that increasing n_z improves accuracy only up to a certain threshold, beyond which further refinement yields negligible benefits. This suggests that an iterative scheme, analogous to the single crystal implementation, could provide a more efficient and stable approach for the stack case in future developments.

The insufficiency of the current method to enforce proper boundary conditions likely originates from the treatment of coupling vectors. In the current formulation, coupling vectors are applied simultaneously to both forward- and backward-propogating channels within the same equation. This approach effectively locks the system into a constrained approximation together with the usage of predetermined incoming beams that fails to reproduce the necessary reflection dynamics. A more promising strategy would be to decouple the forward and backward channels, enforcing boundary conditions separately for each. Such a modification would allow for a consistent description of reflection coupling across multiple interfaces and could resolve the observed discrepancies.

With this revised strategy, the matrix formalism given in Equation 2.72 generalizes to

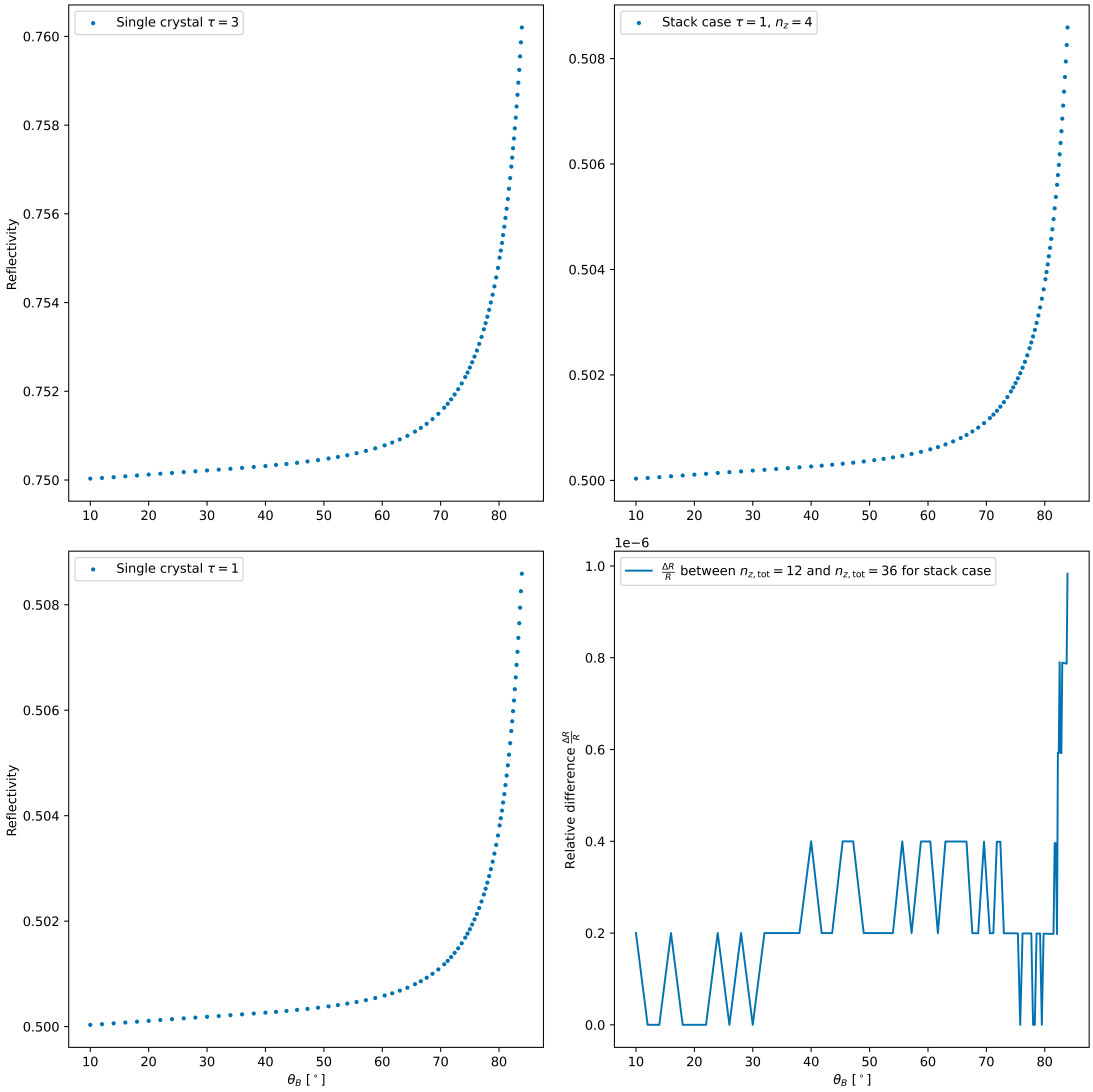

Figure 4.11: Total reflectivity at the Bragg condition $\theta_{\mathrm{in}} = \theta_B$ for different crystal configurations. The left panels show the results for a single crystal with $\tau = 3$ (top left) and $\tau = 1$ (bottom left). The right panels display the corresponding results for a stack of three crystals with $\tau = 1$ and discretization parameter $n_{z,\mathrm{tot}} = 12$ (top right). For comparison, the relative change in reflectivity between the stack cases with $n_{z,\mathrm{tot}} = 12$ and $n_{z,\mathrm{tot}} = 36$ is shown in the bottom right panel. Number of bins chosen as $n_i = 91$ and n_j=1.

the following form

$$\begin{pmatrix} L^0 & 0 & 0 & 0 & 0 & 0 & 0 \\ 0 & L^1 & 0 & 0 & 0 & 0 & 0 \\ 0 & 0 & L^2 & 0 & 0 & 0 & 0 \\ I_f^1 & -I_f^2 & 0 & 1 & 0 & 0 & 0 \\ 0 & I_f^1 & -I_f^2 & 0 & 1 & 0 & 0 \\ I_b^1 & -I_b^2 & 0 & 0 & 0 & 1 & 0 \\ 0 & I_b^1 & -I_b^2 & 0 & 0 & 0 & 1 \end{pmatrix} \begin{pmatrix} y^0 \\ y^1 \\ y^2 \\ \lambda^1 \\ \lambda^2 \\ \lambda^3 \\ \lambda^4 \end{pmatrix} = \begin{pmatrix} 0 \\ 0 \\ 0 \\ 0 \\ 0 \\ 0 \\ 0 \end{pmatrix}. \tag{4.1}$$

This extended formulation introduces explicit separation of the forward (I_f) and backward (I_b) coupling vectors, ensuring that boundary conditions are properly enforced at each interface. Such an approach represents a promising pathway toward resolving the reflection coupling problem and achieving a physically consistent description of mosaic crystal stacks.

5 Conclusion and Outlook

In this work, we have developed and tested a framework for modeling scattering in the stack of mosaic crystals based on a Bragg matrix formalism, with particular focus on the effects of crystal tilting.

The transformation of the polar deflection and azimuthal shift functions was derived and validated, demonstrating consistency with the expected scattering geometry. For tilted crystals, these functions correctly reproduced the angular redistribution of scattered beam, especially in the physically relevant azimuthal regime weighted by the von Mises-Fisher distribution.

the construction of Bragg matrices for tilted crystals further confirmed that the formalism reproduces the correct Bragg reflection conditions in the local reference frame. However, an important limitation was identified: duplicate entries in the tilted Bragg matrices introduced unphysical scattering channels, which violated probability conservation and led to spurious attenuation. Thus issue was clearly manifested in the reflectivity calculations. While the normal oriented crystal showed physically consistent reflectivity and transmission with negligible attenuation, the tilted cases exhibited strong artificial losses, preventing a reliable extraction of physically meaningful results. The analysis traced these problems back to the computational implementation of the Bragg matrix, particularly the reflection and bisection routines, rather than the theoretical framework itself.

Finally, a preliminary study of stacked crystals highlighted the importance of reflection coupling across interfaces. The current model, which lacks an explicit reflection coupling element, cannot capture the full reflectivity of the stack and underestimates transmission by neglecting internal reflections. Although coupling vectors ensured partial continuity within each crystal, the abscence of interfacial reflection conditions effectively blocked the propogation of reflected flux through the entire system.

Future work should address these limitations along two main directions. First, the implementation of the Bragg matrix for tilted crystals must be revised to eliminate duplicate entries and enforce probability conservation. A practical starting point would be the introduction of assertion checks to verify matrix normalization at each step, combined with a systematic investigation of the origin of duplicate values within the reflection kernel routine. Second, the reflection coupling element should be incorporated into the stack model to ensure continuity of backward-propogating flux across inter-

faces. This improvement will enable a physically consistent description of multi-layer crystal systems, which is essential for modeling PST chopper in spectrometers such as SPHERES at FRM II. Finally, the two components, the tilted crystal formalism and the stack model, should be unified into a single framework to enable realistic simulations of a static PST chopper. Such a framework would then provide the foundation for the more challenging task of simulating the rotating PST chopper, thereby bringing the model closer to direct experimental application.

In conclusion, while the present study has identified important challenges in the implementation, it has also established the theoretical consistency of the tilted crystal formalism and clarified the requirements for extending the Bragg matrix approach to stacked crystal systems. These developments provide a solid foundation for future refinement of the model and its eventual application to quantitative predictions of neutron scattering experiments.

List of Figures

List of Tables

Bibliography

[1] J. Wuttke, A. Budwig, M. Drochner, H. Kämmerling, F.-J. Kayser, H. Kleines, V. Ossovyi, L. C. Pardo, M. Prager, D. Richter, G. J. Schneider, H. Schneider, and S. Staringer. "SPHERES, Jülich's high-flux neutron backscattering spectrometer at FRM II." In: *Review of Scientific Instruments* 83.7 (July 2012). ISSN: 1089-7623. DOI: 10.1063/1.4732806.

[2] F. Bornemann, Y. Y. Li, and J. Wuttke. "Multiple Bragg reflection by a thick mosaic crystal. II. Simplified transport equation solved on a grid." In: *Acta Crystallographica Section A* 76.3 (2020). DOI: 10.23689/fidgeo-4472.

[3] M. Bée. *Quasielastic Neutron Scattering*. Bristol: Adam Hilger, 1988.

[4] T. Springer. "Quasielastic neutron scattering for the investigation of diffusive motions in solids and liquids." In: *Springer Tracts in Modern Physics, Volume 64*. Berlin, Heidelberg: Springer Berlin Heidelberg, 1972, pp. 1–100. ISBN: 978-3-540-37457-2. DOI: 10.1007/BFb0042411.

[5] D. Noferini, B. Frick, M. M. Koza, and M. Karlsson. "Proton jump diffusion dynamics in hydrated barium zirconates studied by high-resolution neutron backscattering spectroscopy." In: *J. Mater. Chem. A* 6 (17 2018), pp. 7538–7546. DOI: 10.1039/C7TA10509F.

[6] B. Frick and L. J. Fetters. "Methyl Group Dynamics in Glassy Polyisoprene: A Neutron Backscattering Investigation." In: *Macromolecules* 27.4 (1994), pp. 974–980. DOI: 10.1021/ma00082a014.

[7] J. S. Gardner, G. Ehlers, A. Faraone, and A. T. Boothroyd. "High-resolution neutron spectroscopy using backscattering and neutron spin-echo spectrometers in soft and hard condensed matter." In: *Nature Reviews Physics* 2 (2020), pp. 103–116. DOI: 10.1038/s42254-019-0128-1.

[8] J. Powles. "The structure of molecular liquids by neutron scattering." In: *Advances in Physics* 22.1 (1973), pp. 1–56. DOI: 10.1080/00018737300101259.

[9] R. Hempelmann. "Quasielastic Neutron Scattering and Solid State Diffusion." In: 13 (Nov. 2000). DOI: 10.1093/acprof:oso/9780198517436.001.0001.

[10] G. Kostorz and S. Lovesey. "Neutron Scattering—General Introduction." In: *Neutron Scattering*. Ed. by G. Kostorz. Vol. 15. Treatise on Materials Science & Technology. Elsevier, 1979, pp. 1–67. DOI: https://doi.org/10.1016/B978-0-12-341815-9.50009-4.

[11] P. Staron, A. Schreyer, H. Clemens, and S. Mayer. *Neutrons and synchrotron radiation in engineering materials science: From fundamentals to applications*. John Wiley & Sons, 2017.

[12] W. Doster, S. Busch, A. M. Gaspar, M.-S. Appavou, J. Wuttke, and H. Scheer. "Dynamical Transition of Protein-Hydration Water." In: *Phys. Rev. Lett.* 104 (9 Mar. 2010), p. 098101. DOI: 10.1103/PhysRevLett.104.098101.

[13] M. Appel, G. Borisov, O. Holderer, M.-S. Appavou, R. Zorn, W. Lehnert, and D. Richter. "Proton diffusion in the catalytic layer for high temperature polymer electrolyte fuel cells." In: *RSC Adv.* 9.65 (2019), pp. 37768–37777. DOI: 10.1039/C9RA06431A.

[14] The Nobel Prize in Physics 1994. *The Nobel Prize in Physics 1994*. https://www.nobelprize.org/prizes/physics/1994/summary/. Accessed: 2025-08-23. The Nobel Prize.

[15] Heinz Maier-Leibnitz Zentrum (MLZ). *SPHERES — Neutron Backscattering Spectrometer*. Accessed: 2025-08-24. 2025. URL: https://mlz-garching.de/spheres.

[16] Heinz Maier-Leibnitz Zentrum (MLZ), Technische Universität München. *Experimental Facilities — MLZ*. https://www.frm2.tum.de/fileadmin/w00bnv/www/Aktuelles___Medien/Broschueren/Sonstige/Experimental-facilities-MLZ-2013.pdf. Accessed: 2025-08-23. 2013.

[17] J. Wuttke. "Multiple Bragg reflection by a thick mosaic crystal." In: *Acta Crystallographica Section A* 70.5 (2014), pp. 429–440. DOI: https://doi.org/10.1107/S205327331400802X.

[18] J. Wuttke. "Multiple Bragg reflection by thick mosaic crystals. III. Deflection by a stack of tilted mosaics." In: *unpublished manuscript* ().

[19] M. Heroux, R. Bartlett, V. Howle, R. Hoekstra, J. Hu, T. Kolda, R. Lehoucq, K. Long, R. Pawlowski, E. Phipps, A. Salinger, H. Thornquist, R. Tuminaro, J. Willenbring, A. Williams, and K. Stanley. "An overview of the Trilinos Project." In: *ACM Trans. Math. Softw.* 31 (Sept. 2005), pp. 397–423. DOI: 10.1145/1089014.1089021.

[20] T. T. P. Team. *The Trilinos Project Website*. 2020.

[21] M. Sala and M. A. Heroux. *Robust algebraic preconditioners using IFPACK 3.0.* Tech. rep. Sandia National Laboratories (SNL-NM), Albuquerque, NM (United States), Dec. 2004. DOI: 10.2172/1127118.

[22] E. Bavier, M. Hoemmen, S. Rajamanickam, and H. Thornquist. "Amesos2 and Belos: Direct and Iterative Solvers for Large Sparse Linear Systems." In: *Scientific Programming* 20 (Jan. 2012), pp. 241–255. DOI: 10.1155/2012/243875.